Systems/Circuits

Neuromodulatory Mechanisms Underlying Contrast Gain Control in Mouse Auditory Cortex

Patrick A. Cody^{1,2,3} and Thanos Tzounopoulos^{1,3}

¹Pittsburgh Hearing Research Center, Department of Otolaryngology, University of Pittsburgh, Pennsylvania 15261, ²Department of Bioengineering, University of Pittsburgh, Pennsylvania 15260, and ³Center for the Neural Basis of Cognition, University of Pittsburgh, Pittsburgh, Pennsylvania 15213

Neural adaptation enables the brain to efficiently process sensory signals despite large changes in background noise. Previous studies have established that recent background spectro- or spatio-temporal statistics scale neural responses to sensory stimuli via a canonical normalization computation, which is conserved among species and sensory domains. In the auditory pathway, one major form of normalization, termed contrast gain control, presents as decreasing instantaneous firing-rate gain, the slope of the neural input-output relationship, with increasing variability of background sound levels (contrast) across time and frequency. Despite this gain rescaling, mean firing-rates in auditory cortex become invariant to sound level contrast, termed contrast invariance. The underlying neuromodulatory mechanisms of these two phenomena remain unknown. To study these mechanisms in male and female mice, we used a 2-photon calcium imaging preparation in layer 2/3 neurons of primary auditory cortex (A1), along with pharmacological and genetic KO approaches. We found that neuromodulatory cortical synaptic zinc signaling is necessary for contrast gain control but not contrast invariance in mouse A1.

Key words: auditory cortex; gain modulation; neuromodulation; sensory adaptation; synaptic zinc

Significance Statement

When sound levels in the acoustic environment become more variable across time and frequency, the brain decreases response gain to maintain dynamic range and thus stimulus discriminability. This gain adaptation accounts for changes in perceptual judgments in humans and mice; however, the underlying neuromodulatory mechanisms remain poorly understood. Here, we report context-dependent neuromodulatory effects of synaptic zinc that are necessary for contrast gain control in A1. Understanding context-specific neuromodulatory mechanisms, such as contrast gain control, provides insight into A1 cortical mechanisms of adaptation and also into fundamental aspects of perceptual changes that rely on gain modulation, such as attention.

Introduction

Neural adaptation enables the brain to efficiently process sensory signals amid changing environments (Schwartz and Simoncelli, 2001; Carandini and Heeger, 2011; Wen et al., 2012). In the visual system, stimulus-response functions shift with respect to average light intensity to ensure neurons are most sensitive along the relevant light range (Carandini and Heeger, 2011). In the auditory system, when the mean and variance of sound levels

Received Oct. 12, 2021; revised May 11, 2022; accepted May 11, 2022.

Author contributions: P.A.C. and T.T. designed research; P.A.C. performed research; P.A.C. analyzed data; P.A.C. wrote the first draft of the paper; P.A.C. and T.T. edited the paper; P.A.C. and T.T. wrote the paper.

This work was supported by N.I.H. grants T32 DC011499 (P.A.C.) and R01 DC007905 (T.T.), and NSF grant NSF-IOS-1655480 (T.T.); and NSF-IOS-1655480 to T.T. We thank Dr. Ross Williamson for helpful discussions and critical reading of the manuscript.

The authors declare no competing financial interests.

Correspondence should be addressed to Thanos Tzounopoulos at thanos@pitt.edu or Patrick A. Cody at pac94@pitt.edu.

https://doi.org/10.1523/JNEUROSCI.2054-21.2022 Copyright © 2022 the authors

change over time, the neuronal sound input level-response functions adapt accordingly to maintain dynamic range across the most relevant sound levels (Dean et al., 2005; Wen et al., 2009). In more complex environments, increases in the variability of sound level (contrast) induce a decrease in the slope of the neural input-output relationship, a gain reduction, to efficiently maintain stimulus discriminability (King and Walker, 2020). This contrast gain control is achieved via a canonical neural computation, normalization (Carandini and Heeger, 2011), which is conserved among species (Rabinowitz et al., 2011; Cooke et al., 2018; Lohse et al., 2020) and sensory domains (Schwartz and Simoncelli, 2001; Olsen et al., 2010; Carandini and Heeger, 2011; Rabinowitz et al., 2011). As such, normalization relies on diverse circuits and mechanisms, and different brain regions or different species may implement it with different available components. In the auditory pathway, sound contrast gain control is evident as early as the inferior colliculus, and continues in comparable strength to thalamus and finally into auditory cortex (ACtx) (Lohse et al., 2020). Along this hierarchy, differences in the underlying cellular architecture, adaptation time, and response properties suggest unique contrast adaptation mechanisms along the auditory pathway (Lohse et al., 2020) that are not simply inherited from subcortical nuclei. The normalization associated with contrast gain control depends on parvalbumin expressing (PV) neurons in visual (Wilson et al., 2012), but not in ACtx (Cooke et al., 2020), supporting the idea that, although normalization is a canonical computation, it is not the outcome of a canonical circuit or mechanism. Moreover, uniquely in the ACtx, additional mechanisms contribute to cortical sound contrast adaptation, as the mean firing rates during sustained sound remain invariant to contrast (Lohse et al., 2020), termed contrast invariance. Importantly, sound contrast adaptations account for changes in perceptual judgments in humans (Lohse et al., 2020) and mice (Angeloni et al., 2021); however, the underlying neuromodulatory mechanisms remain poorly understood.

Recent work using 2-photon calcium imaging (2PCI) in awake mice has established synaptic zinc as a key neuromodulator of cortical sound processing (Anderson et al., 2017; Kumar et al., 2019). Critical to the current study, synaptic zinc signaling modulates the gain of cortical sound-evoked responses (Anderson et al., 2017) and contributes to frequency selectivity in the primary ACtx (A1) (Kumar et al., 2019). These effects are eliminated in ZnT3 KO mice that lack the vesicular zinc transporter (ZnT3), which loads zinc into synaptic vesicles (Palmiter et al., 1996; Cole et al., 1999; Anderson et al., 2017; McAllister and Dyck, 2017a). In the absence of cortical synaptic zinc, ZnT3 KO mice exhibit reduced acuity for detecting changes in sound frequency (Kumar et al., 2019). At the level of synaptic transmission and neuromodulation, vesicular (synaptic) zinc is released with glutamate and GABA to inhibit GluN2A-containing NMDARs and AMPARs and potentiate GABARs (Ruiz et al., 2004; Paoletti et al., 2009; Vergnano et al., 2014; Anderson et al., 2015; Kalappa et al., 2015; Kouvaros et al., 2020; Krall et al., 2020). Together, these results have unmasked a fundamental role of zinc signaling in the fields of synaptic transmission and A1 sound processing.

Here, we probed the influence of zincergic neuromodulation on the two phenomena of cortical sound contrast adaptation: contrast gain control and contrast invariance. To study these phenomena, we used an awake 2PCI preparation to assay principal, PV, and somatostatin-expressing (SOM) cell response properties with respect to low and high spectrotemporal sound level contrast. To determine the dependence of these adaptations on synaptic zinc, we used a combined pharmacological (Pan et al., 2011) and genetic KO approach (Cole et al., 1999). Our results support that A1 contrast gain control is under the neuromodulatory control of synaptic zinc signaling.

Materials and Methods

Animals. Mice were handled, anesthetized, and killed according to methods approved by the University of Pittsburgh Institutional Animal Care and Use Committee. The approved Institutional Animal Care and Use Committee protocol numbers that were used for this study were as follows: 17071036 and 17127808. We used 44 male (M) and female (F) mice: 6 F and 9 M ICR/HaJ (The Jackson Laboratory strain #009122) mice for contrast gain control and contrast invariance experiments in putative principal cells expressing CaMKII as well an additional 3 F and 2 M mice for Figure 1p and 2 M mice for Figure 1m. Homozygous mice expressing Cre recombinase in PV- or SOM-expressing cells (PV-Cre and SOM-Cre mice; The Jackson Laboratory strain #017320 and #013044, respectively) were used for the PV and SOM cell experiments

in Figure 5. We used 5 F and 2 M PV-Cre mice as well as 2 F and 5 M SOM-Cre mice. For Figure 4s, t, homozygous mice lacking the vesicular zinc transporter (ZnT3) (Cole et al., 1999), ZnT3-KO mice (2 F and 2 M), were used along with homozygous littermate controls, ZnT3-WT (3 F and 1 M). ZnT3KO/WT mice were backcrossed with C57BL6/J mice at least 5 times from the founder line (The Jackson Laboratory strain #005064) and thus considered congenic with C57BL6/J mice. Experiments using these mice were done blind to KO or WT designation. Mice were injected between postnatal day (P) 24 and P30 for viral transduction of the GCaMP6f calcium indicator used for *in vivo* nonanesthetized imaging experiments done at P38-P49.

Stereotaxic adeno-associated virus (AAV) injections. At P24-P30, mice were induced to anesthesia with 3% isoflurane in oxygen, fastened on a stereotaxic frame (Kopf), and maintained at 1.5% isoflurane for intracortical virus injections. A 30-gauge needle was used to bore a \sim 0.4-mm-diameter craniotomy \sim 4 mm lateral to λ above the right ACtx. A pulled glass micropipette (1.2 mm OD, World Precision Instruments) was lowered 100 µm below pia surface into cortex using a micromanipulator (Kopf) to deliver 600 nl of a GCaMP6f virus diluted in PBS. Putative principal cells expressing CaMKII were targeted with AAV9.CaMKII.GCaMP6f.WPRE.SV40 (Addgene 100834; $2-2.5 \times 10^{13}$ GC/ml; diluted at 1:6 in PBS). Cre recombinase expressing cells in PV-Cre or SOM-Cre mice were targeted with AAV9.CAG. FLEX.GCaMP6f.WPRE.SV40 (Addgene 100835; $2-2.5 \times 10^{13}$ GC/ml; diluted 1:1 in PBS). The viral solution was delivered via tubing from a 5 μl glass syringe (Hamilton), backfilled with mineral oil and injected at a rate of 200 nl/min using a motorized syringe pump (World Precision Instruments). The pipette was left in place for 1 min following injection. After retracting the pipette, the scalp surgical area was closed using adhesive and treated with triple antibiotic ointment. For analgesia, mice were injected with 5 mg/kg carprofen intramuscularly following virus injection and 2 consecutive days after surgery interperitoneally.

Acute surgery preparation for in vivo imaging. At P38-P49, mice were induced to anesthesia with 3% isoflurane in oxygen and then transferred to the imaging apparatus in a sound- and light-attenuating chamber and fitted into a head cone delivering 1.5% isoflurane in oxygen throughout surgical preparation. Body temperature was maintained at \sim 37°C via a heat pad with rectal thermistor. Ophthalmic ointment was applied to protect the eyes throughout anesthesia, and 1% lidocaine was injected intramuscularly to numb the surgical site. The skull above the right temporal cortex was exposed with a \sim 1.5 cm incision in the scalp surrounding the right ear. The exposed skull was affixed to a custom imaging mount using adhesive and dental acrylic (Lang) with the head at a 45° angle to the sagittal plane such that the pial surface of the right temporal cortex was perpendicular/transverse to the upright imaging optics. To minimize movement disturbance during imaging, the animal was positioned into a bottomless 50 ml tube (27 mm diameter). Dental acrylic around the affixed skull was formed into a reservoir centered around the imaging area to hold warmed ACSF. Contaminating zinc was removed during ACSF preparation by incubating with Chelex 100 resin (Bio-Rad) for 1 h. Chelex was removed by vacuum filtration; and finally, high purity calcium and magnesium salts were added (99.995% purity; Sigma-Aldrich). The ACSF solution at pH 7.25-7.35 with an osmolarity of ~300 mOsm contained the following ingredients (in mm): 130 NaCl, 3 KCl, 2.4 CaCl₂, 1.3 MgCl₂, 20 NaHCO₃, 3 HEPES, 10 D-

Sound stimulus delivery. Sound was delivered from a calibrated free-field speaker (ES1, Tucker Davis) situated 10 cm from the animal's left ear. Speaker calibration was performed to create a flat speaker response across all frequencies comprising the dynamic random chord (DRC) stimuli (see DRC stimuli). For calibration, microphones with attached pre-amps (1/8 inch 4138-A-015 and 1/4 inch 4954-B, Brüel and Kjær) were calibrated to a 1 kHz pure tone at 94 dB SPL from a reference sound calibrator (Type 4231, Brüel and Kjær) and positioned in the same location as the animal's left ear. Sound stimuli were generated and output voltage was scaled according to calibration data using custom MATLAB (The MathWorks) scripts using the signalObject library for compatibility with the Ephus software (Suter et al., 2010) that was used for sound delivery and synchronized epifluorescence imaging. Digital sound

signals were converted to analog output at 250 kHz (USB-6229, National Instruments) and sent to the ES1 speaker via an ED1 speaker driver (Tucker Davis).

Widefield epifluorescence imaging and analysis for A1 localization. After surgical preparation, transcranial sound-evoked epifluorescence responses were recorded a minimum of 10 min following cessation of isoflurane delivery to localize ACtx and tentatively identify subfields by tonotopic gradients (Linden et al., 2003; Anderson et al., 2017) for mapping a craniotomy for 2-photon imaging. Mice were then reanesthetized with isoflurane, and a \sim 2 mm² craniotomy was made surrounding A1 by scoring the skull with an 18 G syringe needle. Again, at least 10 min following isoflurane cessation and with the skull above the 2-photon imaging area removed, A1 was more precisely localized using the same approach. For mapping tonotopic gradients, we presented 5-6 kHz pure tones at 60 dB SPL while illuminating the imaging area with a blue LED (nominal wavelength, 470 nm; M470L3, Thorlabs). We imaged GCaMP6f emission under a 4× objective (Olympus) through a GFP filter (BrightLine GFP-A-Basic, Semrock) using a cooled CCD camera (Retiga 2000R, Q-imaging). Images were acquired with a 20 Hz frame rate at a resolution of 200×150 pixels using $8 \times$ spatial binning. Each pixel covered an area of 171.1 μ m².

For evaluating tone-evoked epifluorescence responses, we calculated normalized fluorescence change from prestimulus baseline (F_0) at each pixel ($\Delta F/F = (F - F_0)/F_0$). Prestimulus baseline was calculated from a 1 s average of fluorescence intensity before pure tone onset (at 2-3 s during imaging). To assess sound-responsive regions, we applied a two-dimensional 5 Hz low-pass fourth-order Butterworth filter to 10 consecutive frames of % $\Delta F/F$ values following pure tone onset, then averaged frames across time. This poststimulus (5-6 kHz pure tone) temporal average reveals two salient sound-responsive regions corresponding to the low-frequency tonotopic areas of A1 and the anterior auditory field as well as smaller less responsive secondary areas ventral to A1 and anterior auditory field (Linden et al., 2003; Anderson et al., 2017).

DRC stimuli. DRC stimuli were generated to have high or low spectrotemporal sound level contrast with the same mean sound level. DRCs consisted of 28 pure tone frequencies between 5 and 51.874 kHz at 1/8th octave intervals or 29 pure tone frequencies between 5-25 kHz at 1/12th octave intervals (data from both DRC bandwidth conditions were combined in Figs. 1c-p and 2 onward, as both resulted in robust contrast gain control; see Fig. 1q-v; Results). For a single chord lasting 25 ms, sound levels for each frequency were sampled from a uniform distribution. Sound levels for low-contrast DRC were sampled from a narrow uniform distribution between 50 and 60 dB SPL (± 5 dB; $\sigma_L \approx 2.9$ dB SPL), while sound levels for high contrast DRC were sampled from a wider distribution between 40 and 70 dB SPL (\pm 15 dB; $\sigma_{\rm L} \approx 8.7$ dB SPL). Both distributions had the same 55 dB SPL mean (Fig. 1a,b). Overall stimulus sound level was $84.4 \pm 0.6 \, dB$ SPL for low contrast and $87.8 \pm 1.5 \, \mathrm{dB}$ SPL in high contrast. The average sound level difference between stimuli (3.4 dB SPL) is comparable to previous studies (Rabinowitz et al., 2011; Lohse et al., 2020). Pure tones were scaled to output voltage with respect to sampled intensity via speaker response calibration data, then summed across frequency to result in a "chord." Chord amplitude was enveloped with 1/fourth sin² and cos² ramps lasting 5 ms for onset and offset, respectively. Chords were then concatenated across time to generate DRC sound stimuli lasting 8 s. At 0.5 or 2 s, chord amplitude was set to 0 V for 400 ms and instead a 70 dB SPL pure tone lasting 400 ms was inserted within this gap (Fig. 1c). Four stimuli were generated for each pure tone frequency (5-51.874 kHz at 1/8th octave intervals), contrast (low, high), and onset (0.5, 2 s) combination.

2PCI. We imaged sound-evoked responses from single cells with 2PCI before (control [CTRL]) and after injecting ZX1 (Pan et al., 2011) (a fast extracellular high-affinity zinc-specific chelator) solution or ACSF solution. Before imaging, we inserted a pulled glass micropipette just below the pial surface at the edge of the craniotomy within ACtx. The pipette contained 100 μm ZX1 and 50 μm AlexaFluor-594 in ACSF (herein referred to as ZX1 solution) or just 50 μm AlexaFluor-594 in ACSF (herein referred to as ACSF solution) and was backfilled with mineral oil and connected to a 5 μl glass syringe mounted in a motorized syringe pump (World Precision Instruments). After a minimum

of 20 min following cessation of isoflurane, we imaged neurons in L2/3 of A1 at a depth of 180-250 μm. We delivered mode-locked 940 nm infrared laser light (MaiTai HP, Newport) at 100-200 mW intensity through a 40 × 0.8 NA objective (Olympus) using X-Y galvanometric scanning with a motorized moveable objective microscope (Sutter MOM) focused on the craniotomy of the animal on a fixed stage. Green fluorescence signal from GCaMP6f emission was amplified using a photomultiplier tube (Hamamatsu H10770PA-40) behind a green emission filter (FF03-525/50, Semrock) and dichroic splitter (Di02-R561, Semrock). Photomultiplier tube, galvanometric scanning, and shutter signals passed through a BNC-2090A breakout (National Instruments) to a PCI-6110 data acquisition card (DAQ; National Instruments) that was controlled with ScanImage 5.3 (Vidrio Technologies) software and synchronized via hard wire to the stimulus delivery DAQ using the NI-DAQmx driver with a MATLAB API. We collected $145 \times 145 \,\mu m$ images at 256×256 pixel resolution at an effective frame rate of 5 Hz.

Contrast adaptation assay. For each experiment, a given pure tone frequency (as determined during *ad hoc* frequency response area [FRA] mapping; see previous section) was presented in each contrast (low, high) and onset (0.5 s, 2 s) combination in a pseudorandom fashion. For the principal cell cohort with the 5-25 kHz DRC stimulus bandwidth (Fig. 1r), the average pure tone frequency was 15.3 kHz from a range of 5-25 kHz pure tone frequencies. The average pure tone frequency for the 5-52 kHz DRC stimulus bandwidth cohort (Fig. 1s) was 16.9 kHz from a range of 5-31 kHz. Similarly, the range and average for the remaining cohorts are as follows: PV-Cre: 6.5-20 kHz, 11.5 kHz average; SOM-Cre: 5.9-33.6 kHz, 20.9 kHz average; ZnT3-KO: 5.9-28 kHz, 14.6 kHz average; ZnT3-WT: 5.4-36.7 kHz, 16.5 kHz average. For each imaging trace, the DRC sound stimulus was both preceded and followed by 4 s of silence. Traces were interleaved by laser off periods of pseudorandom duration lasting 25-35 s. A minimum of 8 repetitions of each parameter combination was presented both before and after intracortical injection of ZX1 or ACSF solutions into ACtx. Solutions were infused at 30 nl/min to 600 nl for 20 min during which the microscope objective was periodically adjusted to maintain cell position. Postinjection recordings followed once solutions diffused within A1 and the syringe pump were adjusted to 9 nl/min. Following 2PCI, solution diffusion (containing AlexaFluor-594) was confirmed with 4× widefield epifluorescence imaging of the craniotomy using a green LED (nominal wavelength, 530 nm; M530L3, Thorlabs) and Texas Red filter (BrightLine TxRed-A-Basic, Semrock). Mice were then killed, and tails from transgenic mice were saved for genotype confirmation.

FRA mapping. For each experiment, we first mapped FRAs of the neurons in the imaging field. We presented pure tones (linearly ramped at 10 ms) comprising the DRC stimulus (5-51.874 kHz; see DRC stimuli) lasting 400 ms at intensities of 30, 50, and 70 dB SPL, occurring at 0.6 or 1 s within a 3 s interstimulus interval window. We presented a minimum of four repetitions of each frequency/intensity combination across several 3 min imaging intervals separated by laser off periods lasting a minimum of 30 s. We then performed an ad hoc analysis to quickly determine a pure tone frequency that elicits the maximum $\Delta F/F$ response across an average of all cell FRAs collapsed across stimulus intensity. Using custom scripts written in MATLAB, ellipses were drawn around all nonoverlapping cells in plane having a visible doughnutshaped fluorescence signal. Normalized fluorescence change from prestimulus baseline ($\Delta F/F = (F - F_0)/F_0$) was calculated for each cell from mean fluorescence intensity signal within the ellipse bounds (F). Prestimulus baseline (F₀) was calculated as the average cell fluorescence signal (F) across a 600 ms baseline before pure tone onset. Peak $\Delta F/F$ responses for each cell were averaged across stimulus intensity and then averaged across cells to determine the pure tone frequency eliciting the maximum response across cells. For the contrast adaptation assay, this pure tone frequency was then presented following 0.5 or 2 s of contrast DRC sound (see next section). For determining best frequency (BF) and final cell FRA, FRA mapping and contrast adaptation assay data were reanalyzed post hoc with nonrigid motion and neuropil correction as described in the next section (2PCI: processing, inclusion criteria, and analysis). Significant peak Δ F/F responses were calculated as maximum $\Delta F/F$ values within an 800 ms window following pure tone onset that are \geq 2 SDs above F_0 . BF for a given cell was determined as the frequency eliciting the largest response averaged across the stimulus intensities.

2PCI: processing, inclusion criteria, and analysis. For a given experiment, 2PCI frames were concatenated for all traces across time and aligned using nonrigid motion correction via the NoRMCorre MATLAB toolbox (Pnevmatikakis and Giovannucci, 2017). Ellipses were manually drawn around nonoverlapping cells (as described in FRA mapping), and contamination from surrounding neuropil (in the form of time varying fluorescence intensity) obtained using the FISSA Python toolbox (Keemink et al., 2018) was scaled by 0.8 (Kerlin et al., 2010; Q. Chen et al., 2020) and removed to obtain motion- and neuropil-corrected average fluorescence intensity across time for each cell. Inclusion criteria: cells were included if deemed tone-responsive. To identify tone-responsive cells ($d' \ge 0$), we used a tone sensitivity index (d') as described previously (Romero et al., 2020). Briefly, for a given cell FRA, we calculated the average response amplitude from responses at and immediately adjacent to the frequency/level combination eliciting the maximum response (average of 5 values if maximum response is observed at dB < 70, 4 values if maximum response is observed at 70 dB). We then averaged the same number of values selected at random frequency/level locations of the FRA. We took the difference of these averages and iterated this process 1000 times. The tone sensitivity index (d') was calculated as the average of the iterated differences. We identified tone-responsive cells with $d' \geq 0$. We then used these tone-responsive cells to assess contrast gain control and contrast invariance. In cases where we indicate trace selection for pure tone responses preceded by DRC contrast (for both contrast gain control and contrast invariance assays), solely cells with significant pure tone responses in both low and high contrast were included (>2 SDs above F_0 for $\Delta F/F$ values within an 800 ms window following pure tone onset). For 2 s DRC durations (pure tone occurring at 2 s), the baseline % Δ F/F is the average of % Δ F/F across 1-2 s. For 0.5 s DRC durations (pure tone occurring at 0.5 s), the baseline % Δ F/F is the average of % Δ F/F across 0.2-0.5 s. For CaMKII-expressing putative principal cells, the average number of total cells imaged per animal is 87.2, and the average number of cells meeting these response criteria per animal is 19.1. This means that, on average, 22.4% of cells from an animal were included. On average, 74.9% of PV cells and 90.5% of SOM cells were included per animal. For all experiments, normalized baseline subtracted fluorescence traces (F(t) = Δ F/F) were first calculated as (F – $F_{0\ DRC}$)/ $F_{0\ DRC}$, where $F_{0\ DRC}$ is the average cell fluorescence intensity before DRC sound onset across -1.2 to 0 s (see, e.g., Fig. 1c). To quantify pure tone responses, for 2 s DRC duration experiments, we calculated F (t) – $F_{0 \text{ PT}}$, where $F_{0 \text{ PT}}$ is the average of F(t) across 1-2 s. For 0.5 s DRC duration experiments, we calculated F(t) - F_{0 PT} with F_{0 PT} as the average of F(t) across 0.2-0.5 s. We used the same two-step approach to calculate both the DRC cut-out (Fig. 1m) and DRC contrast switch responses (Fig. 1p). For the DRC cut-out response in Figure 1m, after 2 s of DRC, no sound is presented for 400 ms (same duration as the duration of the pure tone stimulus in Fig. 1c), and the DRC resumes at 2.4 s after the DRC cut-out. For these responses, we calculated F(t) - $F_{0_DRC_cut-out}$ where $F_{0_DRC_cut-out}$ is the average of F(t) across 1-2 s. For the DRC contrast switches in Figure 1p, we calculated F(t) – F_0 $\Delta \sigma$ where $F_{0 \Delta \sigma}$ is the average of F(t) across 8-10 s.

Statistical analysis. All statistical analyses were performed in MATLAB; % Δ F/F data are presented as mean \pm SEM. Responses to sustained contrast and contrast scaling factors are presented as boxplots in violin plots. For a given analysis, an Anderson–Darling test was first performed to determine whether data arose from a normal distribution. Data that failed to reject the null hypothesis were considered normally distributed. In this case, one-sample t tests were used to determine significance in single samples. For two-sample comparisons, paired and unpaired t tests were used for within- or between-subject data, respectively. All t tests were two-tailed. For comparison between multiple groups having within-subject factors (see Fig. 6b,e), a repeated-measures two-way ANOVA test was used. Bonferroni corrections were used for multiple two-sample $post\ hoc$ comparisons among sample groups; the significance level (α = 0.05) of the test was corrected via scaling by the reciprocal of the number of comparisons. Nonparametric comparisons

were used on data for which the Anderson–Darling null hypothesis was rejected. The Wilcoxon signed-rank test was used for one-sample comparisons. A permutation test (Wasserman, 2004) was used for two-sample comparisons. Samples for which <5000 of 100,000 random permutations of the data resulted in mean differences greater than the observed difference in sample means were considered significant (p < 0.05).

Results

2PCI assay for adaptation to sound level contrast in A1 L2/3 principal neurons

To interrogate neuromodulatory and cellular signaling mechanisms underlying contrast adaptation in A1 L2/3 principal neurons, we devised an in vivo awake 2PCI assay in mice. Our nonparametric approach is based on previous electrophysiological analyses that do not rely on a parametric firing-rate model (Rabinowitz et al., 2011; Cooke et al., 2020). We used 2PCI to record sound-evoked calcium fluorescence transients from single principal cells in awake head-fixed mice that express the GCaMP6f calcium indicator. For these experiments, we injected ACtx with an AAV that drives GCaMP6f expression under control of the CaMKII promoter. For each recording, we first localized A1 using wide-field 4× epifluorescence calcium imaging by comparing the response with a 5-6 kHz pure tone at 50-60 dB SPL with established tonotopic maps of mouse ACtx (Linden et al., 2003; Anderson et al., 2017; Romero et al., 2020). We then mapped single-cell FRAs for a single field of cells within A1 L2/3 under 2PCI at 40 ×. Then, to identify the pure tone frequency with the maximum response, we averaged the FRAs across these cells. To assess contrast adaptation, we presented this pure tone at 70 dB SPL following 2 s of DRCs having either low or high spectrotemporal sound level contrast (Fig. 1a). Sound level varied across both frequency and time (Fig. 1a,b), at $\pm 5\,\mathrm{dB}$ ($\sigma \approx$ 2.9 dB) for low- and ± 15 dB ($\sigma \approx 8.7$ dB) for high-contrast DRCs, but both DRC stimuli had the same mean sound level of 55 dB (DRC stimuli). Figure 1c shows the time course of the 2PCI assay and illustrates cell averages of fluorescence response traces during low (blue) and high (orange) contrast stimuli, covering from 1.2 s before the DRC onset until the end of the 8 s DRC stimulus (n = 244 cells, 15 mice). Traces were baseline (F_0) subtracted and normalized, $\Delta F/F = (F - F_0)/F_0$, where F_0 is the mean fluorescence before DRC onset (-1.2 to 0 s). We used this assay to assess two phenomena of contrast adaptation: contrast gain control and contrast invariance (Fig. 1c, gray boxes). First, we assessed contrast gain control by comparing responses with pure tones preceded by low versus high contrast (Fig. 1c, left gray box; for different calculation of the pure tone fluorescent responses, see Fig. 1*d*,*e*). Second, we assessed contrast invariance by comparing mean fluorescence responses during sustained low- versus high-contrast DRC segments (Fig. 1c, right gray box at 6-8 s; Fig. 1f).

Consistent with previous studies assessing contrast gain control (Rabinowitz et al., 2011; Cooke et al., 2020), neural responses to pure tones in high contrast are reduced compared with responses in low contrast (Fig. 1c, left gray box). To quantify the pure tone fluorescent responses, we calculated F(t) – F_{0_PT}, where F_{0_PT} is the average of F(t) in Figure 1c across 1-2 s (Fig. 1d). We plotted each cell's average peak pure tone response following 2 s of low contrast against its response following 2 s of high contrast (Fig. 1e) and found that response amplitudes were significantly reduced when preceded by high contrast (p = 10e-6, permutation test; p = 274 cells, 15 mice; slope 95% CI: 0.68-0.73). The regression line and 95% CI in Figure 1e and subsequent

scatterplots are only used for depictive purposes; coloration other than gray represents the direction of a significant effect of contrast as measured by a permutation test. Together, using a 2PCI assay, we measure contrast gain control that is consistent with previous electrophysiological studies (Rabinowitz et al., 2011; Cooke et al., 2018, 2020).

We next determined whether our assay recapitulates a second phenomenon of contrast adaptation, cortical contrast invariance. We hypothesized that mean % Δ F/F activity during the sustained contrast DRC segment (Fig. 1c, right gray box at 6-8 s) would not differ with respect to contrast, as seen with mean A1 firing rates in previous electrophysiological studies (Lohse et al., 2020). To assess contrast invariance with our assay, we isolated % Δ F/F activity during sustained DRC presentation within a 2 s epoch that sufficiently follows pure tone response decay (6-8 s). Temporal averages of cell % Δ F/F traces in Figure 1*c* during this sustained contrast epoch (6-8 s) did not differ with respect to contrast (Fig. 1f, violin plot, p = 8.98e-01, permutation test; n = 244 cells from 15 mice). This result suggests that the second epoch of our 2PCI assay during sustained contrast DRCs (Fig. 1c, right gray box; Fig. 1f) reproduces a second phenomenon of contrast adaptation, cortical contrast invariance.

We noticed that the baseline traces showed a run-down before the pure tone response and a milder run-up after the pure tone response (Fig. 1c). When we averaged the traces that showed pure tone response amplitudes that were smaller than 2 SDs of the baseline in either low or high contrast, we noticed that there was a significant run-down and run-up of the baseline before and after the pure tone response, respectively (Fig. 1g). We therefore decided to exclude these traces to test whether the average baseline traces became more stable, and whether the main effects of contrast gain control and contrast invariance were still observed. After removal of those traces, we found that the baseline traces were more stable (Fig. 1i). Importantly, we found that contrast gain control (Fig. 1j,k) and contrast invariance (Fig. 10) were still observed, suggesting the robustness of these two main phenomena of our study (contrast gain control: Fig. 1k, p = 9.99e-6, permutation test; n = 244 cells, 15 mice; slope 95% CI: 0.73-0.79; contrast invariance: Fig. 10, violin plot, p = 4.05e-1, permutation test; n = 244 cells from 15 mice). Given the improvement of baseline responses, we opted to illustrate the traces with the aforementioned trace selection throughout the manuscript, except for Figures 1 and 4 where we show traces and analyses for both procedures. Because we understand the potential problems of this trace selection, we also performed for all figures the analyses without any trace selection. All values and stats for these analyses are reported in Table 1. In all cases, we observed similar results with these two different types of analyses, further supporting the robustness of our findings.

To assess whether contrast gain control is consistent at the animal level, we plotted pure tone responses in low versus high contrast using the mouse as the individual unit of analysis (Fig. 1l, average across cells). The main effect of contrast is consistent: amplitudes of neural responses to pure tones in high contrast are reduced compared with responses in low contrast (p = 3.52e-2, permutation test, N = 15 animals). Thus, using this 2PCI assay, we observe contrast gain control at both the cellular and animal level.

To control for a potential effect of the cut-out in DRC sound during the 400 ms pure tone, we conducted the same experiment as in Figure 1c (no trace selection), but without a pure tone. Namely, at 2 s into the DRC stimulus, the DRC was cut-out and no sound was presented for 400 ms (same duration as the

duration of the pure tone stimulus in Fig. 1c). We used the same two-step approach to calculate DRC cut-out % Δ F/F responses as was used for the pure tone responses in Figure 1d. Accordingly, we first calculated F(t) as (F - F_{0_DRC})/F_{0_DRC}, where F_{0 DRC} is the average cell fluorescence intensity before DRC sound onset across -1.2 to 0 s (as in Fig. 1c). DRC cut-out % Δ F/F responses were then calculated as F(t) – F_{0 DRC cut-out}, where $F_{0_DRC_cut-out}$ is the average of F(t) across 1-2 s (Fig. 1m, top; 172 cells from 2 mice). We compared the average DRC cutout responses between low and high contrast across 2.4-2.6 s, where we observe peak pure tone responses in Figure 1d, and plotted them in the violin plot shown in Figure 1m. We did not observe an effect of contrast on these responses (p = 0.45, permutation test). The plot in Figure 1*n* includes the positive pure tone responses and negative cut-out responses on the same plot, and shows that pure tone responses (also shown in Fig. 1c,d) do not reflect offset responses. Together, these results support that the effect of contrast on pure tone response amplitude is not attributable to the cessation of the DRCs during the 400 ms of pure tone presentation, and thus further validate our 2PCI assay for studying contrast gain control mechanisms.

In Figure 10, we show that the 6-8 s sustained contrast DRC segment recapitulates contrast invariance. However, it does not clearly reveal the time course of response adaptation to comparable levels after a change in contrast, as observed in previous electrophysiological studies (Lohse et al., 2020). To account for this, we performed additional experiments in which we recorded % Δ F/F activity after a change in contrast from low to high and from high to low (Fig. 1p), as done in previous studies (Cooke et al., 2018; Lohse et al., 2020). In this new cohort, we first calculated F(t) as before: $(F - F_{0_DRC})/F_{0_DRC}$, where F_{0_DRC} is the average cell fluorescence intensity before DRC sound onset across -1.2 to 0 s. For quantification of % $\Delta F/F$ changes because of the contrast switch, we then calculated F(t) – $F_0 \Delta \sigma$ where $F_0 \Delta \sigma$ is the average of F(t) across 8-10 s (Fig. 1p, top). The change from low to high contrast (at 10 s) resulted in initially larger responses that fully adapted and returned to low contrast response levels within 1.4 s (as seen with the 11.4-12 s temporal average in Fig. 1p, bottom, violin plot; p = 0.10, permutation test; n = 208 cells, 5 mice). Consistent with Figure 1c (right gray box) and Figure 1f, mean responses during sustained DRC segments remained invariant to contrast. Thus, despite the longer adaptation time that is likely because of the calcium imaging signal, our results assessing contrast invariance are consistent with electrophysiology data (Lohse et al., 2020).

To examine the dependence of contrast adaptation on sound context bandwidth, we used the 2PCI assay to compare contrast gain control (as in Fig. 1k) and contrast invariance (as in Fig. 1o) between DRC stimuli (Fig. 1q) with either a narrow (Fig. 1r, left; 5-25 kHz) or wide (Fig. 1s, right; 5-52 kHz) bandwidth. To perform this comparison, we separated the data in Figure 1i-o, which contain combined data from both 5-25 kHz and 5-52 kHz DRC bandwidth conditions, and we assessed sound contrast adaptation in each condition (Fig. 1q-v). We observed significantly reduced pure tone response amplitudes in high contrast in both bandwidth conditions (Fig. 1r, 5-25 kHz DRC; p = 9.99e-6, permutation test; slope 95% CI: 0.71-0.80; n = 144 cells from 8 mice; Fig. 1s, 5-52 kHz DRC; p = 3.09e-3, permutation test; slope 95% CI: 0.72-0.83; n = 100 cells from 7 mice). To quantify contrast gain control and directly compare it between the DRC bandwidth conditions, we calculated the contrast scaling factor, defined as the population mean of individual cell average peak responses in low contrast divided by average peak responses in

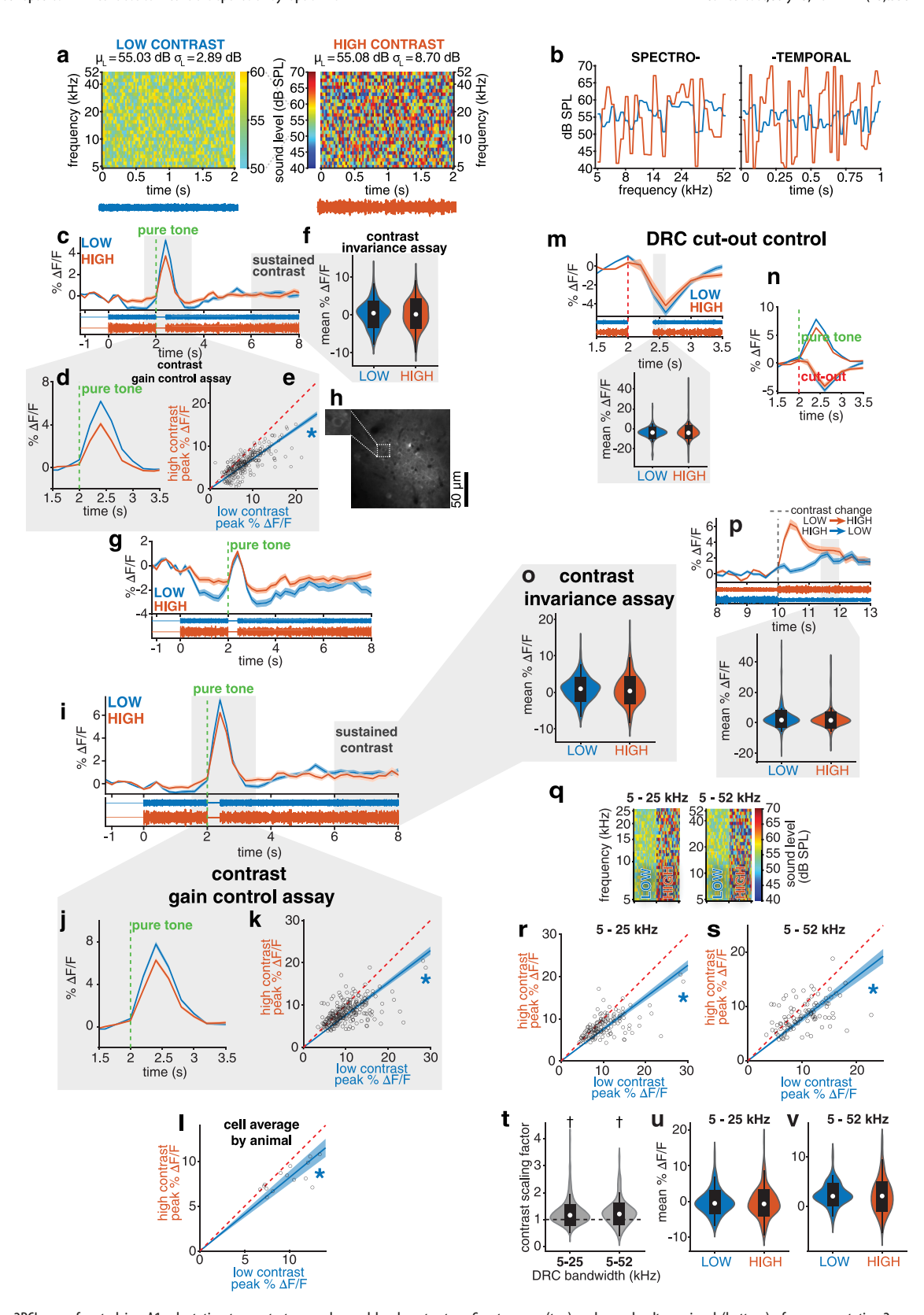


Figure 1. 2PCI assay for studying A1 adaptation to spectrotemporal sound level contrast. \boldsymbol{a} , Spectrogram (top) and sound voltage signal (bottom) of a representative 2 s epoch from low (left; blue) and high (right; orange) contrast DRC stimuli. For each 25 ms time bin column in the spectrogram, sound levels for each frequency (depicted by color) are sampled from a narrow (low contrast; \pm 5 dB; left color bar) or wide (high contrast; \pm 15 dB; right color bar) uniform distribution with the same 55 dB SPL mean. \boldsymbol{b} , Sound level (dB SPL) plotted against frequency (left) and time (right) to depict low (blue) and high (orange) spectral and temporal contrast, respectively, of the DRC stimuli. \boldsymbol{c} , Mean \pm SEM of % Δ F/F traces from A1 principal cells (top) during low (blue) and high (orange) contrast stimuli with a 400 ms pure tone occurring at 2 s after the initiation of the DRC stimulus. Baseline, F_0 , for % Δ F/F calculated before DRC onset at -1.2 to 0 s. Bottom, Representative sound voltage signals. \boldsymbol{d} , Mean \pm SEM of % Δ F/F traces during the pure tone epoch calculated as $F(t) - F_0$ using F(t) in \boldsymbol{c} and F_0 as F(t) at 1-2 s. \boldsymbol{e} , Scatterplot of each cell's mean peak % Δ F/F pure tone response in low versus high contrast (p = 10e-6, permutation test; slope 95% CI: 0.68-0.73; n = 274 cells, 15 mice; the regression line in this and in subsequent scatterplots is only used for depictive purposes). \boldsymbol{f} , Violin plot of temporal averages of % Δ F/F responses during the sustained contrast epoch at 6-8 s for low (blue)

high contrast (Fig. 1*t*). We determined contrast gain control to be evident if the contrast scaling factor is significantly >1. Both DRC bandwidth conditions exhibited contrast gain control (5-25 kHz: p=6.22e-12; 5-52 kHz: 6.86e-8; Wilcoxon signed-rank tests), and contrast gain control did not differ between the two DRC bandwidth conditions (Fig. 1*t*; p=5.74e-1, permutation test). We additionally assessed contrast invariance, as in Figure 1*o*, and found that it was evident in both DRC bandwidth conditions (Fig. 1*u*,*v*). Responses to the 6-8 s sustained contrast epoch did not differ between contrast in either DRC bandwidth condition (5-25 kHz, Fig. 1*u*, p=7.04e-1, permutation test; 5-52 kHz, Fig. 1*v*, p=5.05e-1, permutation test). This result supports that the scaling effect of contrast on L2/3 A1 principal cell responses to pure tones is robust to a more than halving of the contrast DRC bandwidth.

To assess whether the effect of contrast is dependent on the duration of the contrast sound before the pure tone, we performed the same assay as in Figure 1i but with pure tones occurring 0.5 s after low- or high-contrast sound (Fig. 2a). To quantify responses to pure tones after a 0.5 s DRC duration, we calculated F(t) – F_{0_PT} with F(t) in Figure 2a and F_{0_PT} as the average of F(t) across 0.2-0.5 s for the 0.5 s DRC duration (Fig. 2b). We plotted each cell's average peak pure tone response following 0.5 s of low-contrast against its response following 0.5 s of high contrast (Fig. 2c) and found that response amplitudes did not significantly differ between contrast (p = 8.52e-1, permutation test; slope 95% CI: 0.78-0.90; n = 176 cells from 12 mice).

and high (orange) contrast (violin plot, p = 4.05e-1, permutation test; n = 274 cells from 15 mice). \mathbf{q}_i Average of nonsignificant traces (traces in which the pure tone response did not exceed 2 SDs of the trace baseline, 255 cells had at least one trace with nonsignificant response in low contrast, and 272 cells had at least one response in high contrast). h, Representative image of 2-photon field of view (FOV) at 145 \times 145 μ m showing A1 L2/3 CaMKII expressing principal neurons. i, Same as in c, but after removing traces shown in g. j, Same as in d, but after removing traces shown in g. k Same as in e, but after removing traces shown in q (p = 9.99e-6, permutation test; slope 95% CI: 0.73-0.79; N = 244 cells from 15 mice. I, Scatterplot of peak pure tone % $\Delta F/F$ responses in low versus high contrast using the mouse as the individual unit of analysis (average across cells; p = 3.53e-2, permutation test; slope 95% CI: 0.75-0.89; N=15 animals). m, Top, Mean \pm SEM of % Δ F/F traces in low and high contrast during a 400 ms cut-out in DRC sound at 2 s (instead of a pure tone) calculated as $F(t) - F_{0_DRC_cut-out}$, where F(t) is $(F - F_{0_DRC})/F_{0_DRC}$, F_{0_DRC} is the average cell fluorescence intensity before DRC sound onset across -1.2 to 0 s (as in Fig. 1c), and $F_{0_DRC_cut-out}$ is F(t) at 1-2 s. Bottom, Representative sound voltage signals. m, Bottom left, Violin plot of temporal averages of % Δ F/F responses at 2.4-2.6 s for low and high contrast (at which peak pure tone responses are observed in \boldsymbol{c} and \boldsymbol{d}) (p=4.5e-1, permutation test; N = 172 cells from 2 mice). White dot represents median. Thick black line indicates interquartile range. Contour lines indicate data distribution. n, Plot represents both positive pure tone responses and negative DRC cut-out responses on the same plot for scale. o, Same as in f, but after removing traces shown in g (p = 4.05e-1, permutation test; N = 244 cells from 15 mice). p, Top, Mean \pm SEM of % Δ F/F traces (top) during a change in sound level contrast from low to high (orange) and high to low (blue). Calculated as $F(t) - F_0$ where F(t)is $(F - F_0)_{DRC}$ with F_0 _DRC as F at -1.2 to 0 s and F_0 as F(t) before contrast change at 8-10 s. Bottom, Representative sound voltage signals. \boldsymbol{p} , Bottom, Violin plot of temporal averages of % Δ F/F responses during 11.4-12 s DRC segment of low or high contrast (p = 0.10, permutation test; N = 208 cells from 5 mice). **q**, Representative low and high contrast DRC stimuli with bandwidths of 5-25 kHz (left) 5-52 kHz (right). r, Same as in k, but solely using 5-25 kHz DRC bandwidth (N = 144 cells from 8 mice; p = 9.99e-6, permutation test; slope 95% CI: 0.71-0.80). **s**, Same as in k, but solely using 5-52 kHz DRC bandwidth (N = 100 cells from 7 mice; p = 3.09e-3, permutation test; slope 95% CI: 0.72-0.83). t, Violin plot of cell contrast scaling factors (cell's average peak low/peak high % Δ F/F pure tone response) with regard to DRC stimulus bandwidth (5-25 vs 5-52 kHz: p = 5.74e-1, permutation test). †Significant difference from 1 via Wilcoxon signed-rank test (5-25 kHz: p = 6.22e-12; 5-52 kHz: 6.86e-8). **u**, Same as in **r**, N = 144 cells from 8 mice (p = 7.04e-1, permutation test). **v**, Same as in **s**, N = 100 cells from 7 mice (p = 5.05e-1, permutation test). For scatterplots, blue asterisks (*) indicate p < 0.05 via permutation test. Blue fitted regression line and 95% CI represent direction of contrast effect.

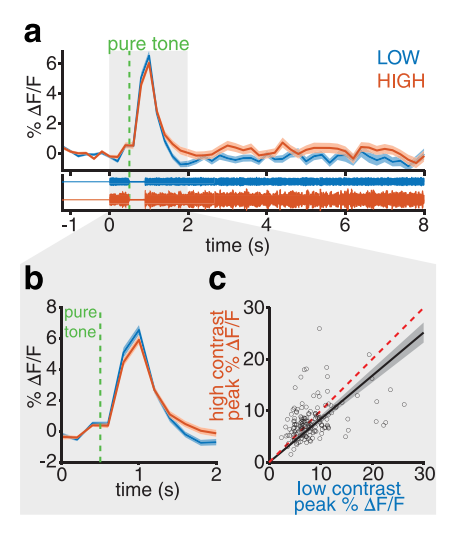


Figure 2. Contrast gain control, as assessed by a 2PCI assay in A1 principal cells, depends on the duration of the contrast sound. \boldsymbol{a} , Mean \pm SEM of % Δ F/F traces from A1 principal cells (top) during low (blue) and high (orange) contrast stimuli with a 400 ms pure tone occurring at 0.5 s after the initiation of the DRC stimulus. Baseline, F₀, for % Δ F/F calculated before DRC onset at -1.2 to 0 s. Bottom, Representative sound voltage signals. \boldsymbol{b} , Mean \pm SEM of % Δ F/F traces during the pure tone epoch calculated as F(t) - F₀ using F(t) in \boldsymbol{a} and F₀ as F(t) at 0.2–0.5 s. \boldsymbol{c} , Scatterplot of each cell's mean peak % Δ F/F response to pure tone after 0.5 s DRC of low versus high contrast (p=8.52e-1, permutation test; slope 95% CI: 0.78–0.90; N=176 cells from 12 mice).

Together, the pure tone response epoch of our 2PCI assay reveals a duration-dependent effect of preceding context contrast that is consistent with previous electrophysiology studies (Rabinowitz et al., 2011).

Because neurons are most sensitive to changes in contrast within the frequency bandwidth at which they are most responsive (Rabinowitz et al., 2012), we explored the frequency dependence of contrast gain control with our 2PCI assay. For each recorded field of cells, a given cell's BF, the frequency that elicited the maximum response across an average of presented sound levels, is at some octave difference from the pure tone frequency used to assess contrast gain control (Fig. 3a, top, representative cell FRA in terms of cell BF octaves from pure tone in assay). We asked whether contrast gain control depends on the distance of the pure tone frequency from cell BFs. We separated our data into cells having BFs within (n = 146 cells from 15 mice) or outside 1 octave (n = 98 cells from same 15 mice) of the pure tone stimulus and plotted each cell's average peak pure tone response following 2 s of low contrast against its response following 2 s of high contrast (Fig. 3b,c). Cells with BFs both within (Fig. 3b; p = 9.99e-6, permutation test; slope 95% CI: 0.73-0.81) and outside (Fig. 3c; p = 3.99e-4, permutation test; slope 95% CI: 0.69-0.80) 1 octave of the pure tone stimulus frequency exhibited contrast gain control. To directly compare contrast gain control between these two conditions, we plotted contrast scaling factors (Fig. 3d, violin plot). We found that contrast scaling factors did not significantly differ between the two conditions (p = 7.95e-1, permutation test) and were significantly >1 in both conditions (within: p = 3.18e-12; outside: 1.30e-7; Wilcoxon signed-rank tests). This result suggests that sound level contrast scales L2/3 A1 principal cell responses to pure tones regardless of the distance of the pure tone from the cell's BF. Together, we established a 2PCI assay that measures two phenomena of cortical contrast adaptation: contrast gain control and contrast invariance. We will use this assay to explore the neuromodulatory mechanisms of cortical adaptation to sound level contrast.

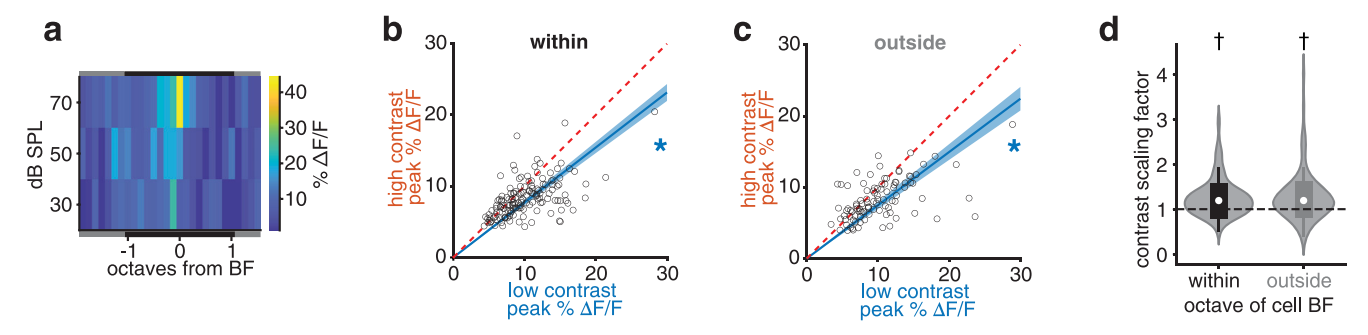


Figure 3. Frequency dependence of contrast gain control, as assessed by a 2PCl assay in A1 principal cells. $\bf a$, Top, FRA from a representative A1 principal cell with frequency on $\bf x$ axis labeled with respect to octaves from cell BF at 18,340 Hz. Color represents mean peak % Δ F/F pure tone response amplitude. $\bf b$, Scatterplot of each cell's mean peak % Δ F/F pure tone response in low versus high contrast from cells with BFs within 1 octave of the pure tone used in the 2PCl assay (p = 9.99e-6, permutation test; slope 95% Cl: 0.73-0.81; N = 146 cells from 15 mice). $\bf c$, Same as in $\bf b$, but from cells with BFs outside 1 octave of the pure tone used in the 2PCl assay (p = 3.99e-4, permutation test; slope 95% Cl: 0.69-0.80; N = 98 cells from 15 mice). $\bf d$, Violin plot of contrast scaling factors from cells with BFs within (black) or outside (gray) 1 octave of the pure tone used in the 2PCl assay (within vs outside: p = 7.95e-1, permutation test). White dot represents median. Thick black line indicates interquartile range. Contour lines indicate data distribution. Both within and outside contrast scaling factors are significantly >1 (p = 3.18e-12, p = 1.30e-7, Wilcoxon signed-rank tests). *p < 0.05 (permutation test). †p < 0.001 (Wilcoxon signed-rank tests).

Contrast gain control in A1 depends on neuromodulatory zinc signaling

Given the lack of knowledge on synaptic neuromodulatory mechanisms underlying contrast gain control, we next investigated the involvement of synaptic zinc, a neuromodulator capable of cell-specific scaling of sound-evoked responses (Anderson et al., 2017). To determine whether synaptic zinc contributes to contrast gain control (Fig. 4a-o; n=150 cells from 9 mice), we first used ZX1, a fast extracellular high-affinity zinc-specific chelator (Pan et al., 2011; Anderson et al., 2015), to inhibit endogenous extracellular zinc signaling (Anderson et al., 2015, 2017; Kumar et al., 2019). We assessed contrast gain control before (CTRL, Fig. 4a-c, lighter shade) and after injecting 100 μ M ZX1 into ACtx (Fig. 4h-j, darker shade). The effect of contrast on pure tone response amplitudes observed in CTRL (Fig. 4c; p = 9.99e-6, permutation test, regression slope 95% CI: 0.71-0.80; Fig. 4d; p = 10.00e-6, permutation test, regression slope 95% CI: 0.67-0.73, n = 179 cells from 9 mice, without trace selection) was no longer evident after ZX1 treatment (Fig. 4j, p = 2.67e-1, permutation test, lack of significance denoted by black/gray coloring of fitted regression line and 95% CI, slope 95% CI: 0.91-1.02; Fig. 4k, p = 8.74e-01, slope 95% CI: 0.89-0.97, n = 179 cells from 9 mice, without trace selection). ZX1 did not, however, affect contrast invariance (Fig. 4e,f,l,m). Specifically, mean % Δ F/F activity during the sustained contrast DRC segment in CTRL (Fig. 4a, right gray box at 6-8 s; Fig. 4e, p = 8.87e-2, permutation test; Fig. 4f, p = 2.48e-01, permutation test, n = 179 cells from 9 mice, without trace selection), remained invariant to contrast after ZX1 injection (Fig. 4h, right gray box at 6-8 s; Fig. 4*l*, p = 1.45e-1, permutation test; Fig. 4m, p = 1.782582e-01, permutation test, n = 179 cells from 9 mice, without trace selection). To directly assess the effect of ZX1 on contrast gain control, we plotted the contrast scaling factor from the same cells before and after ZX1 injection (Fig. 4o, n = 150 cells, 9 mice). We observed a significant decrease in the contrast scaling factor following ZX1 injection (p = 9.99e-6, permutation test), and the contrast scaling factor no longer significantly differed from 1 in the presence of ZX1 (p = 5.03e-2, Wilcoxon signed-rank test). To control for a potential effect of the injection pipette and the injection of a solution volume in cortex, we performed the same assay before and after injection of the vehicle: 50 μ M AlexaFluor-594 in ACSF (Fig. 4p). The contrast scaling factor was significantly >1 both before (p = 9.53e-8) and after vehicle injection (p = 1.61e-4, Wilcoxon) signed-rank tests) and did not significantly differ after injection (Fig. 4p; p = 9.49e-1, permutation test; n = 73 cells from 6 mice). Together, these results suggest that zinc signaling is necessary for cortical contrast gain control, but not for contrast invariance.

To test for potential ZX1 effects on cell FRA (Kumar et al., 2019), we mapped cell FRAs both before and after ZX1 injection. We first measured the effect of ZX1 on BF and found that it did not affect BF across the cell population average (Fig. 4q, $t_{(110)}$ = -0.9184, p = 3.60e-1, one-sample t test; n = 111 cells from 5 mice), suggesting that ZX1 effects on contrast gain control are not because of ZX1 effects on cell FRA. Because principal neuron pure tone responses in silence are modulated by synaptic zinc depending on pure tone distance from cell BF (Kumar et al., 2019), we next limited our analysis to responses from pure tones occurring within one-fourth octave of cell BF in both control and ZX1 conditions (Fig. 4r; n = 69 cells, 5 mice). We observed that the ZX1 effect on the contrast scaling factor persisted (p = 3.41e-2, permutation test) and was not different from that of the entire population average (in Fig. 40). Together, these two analyses suggest that the contribution of endogenous zinc signaling to contrast gain control is unlikely to be attributable to zinc effects on cell tuning.

The effect of endogenous zinc signaling may be attributable to synaptically released ZnT3-dependent vesicular zinc (Cole et al., 1999; Anderson et al., 2017), tonic zinc (Anderson et al., 2015; Perez-Rosello et al., 2015), or both (Krall et al., 2020). To ascertain the source of zinc signaling, we assessed contrast gain control before and after intracortical ZX1 injection (Fig. 4s,t) in WT mice (ZnT3-WT) and KO (ZnT3-KO) mice that lacked ZnT3, and thus synaptic zinc (Cole et al., 1999). We found that contrast gain control was eliminated in ZnT3 KO mice (Fig. 4s; the contrast scaling factors do not significantly differ from 1; CTRL: p = 7.04e-02; ZX1: p = 1.67e-1; Wilcoxon signed-rank tests), and furthermore, that ZX1 did not have any effect on ZnT3-KO mice (p = 8.66e-2, permutation test; n = 61 cells from four mice). This suggests the critical involvement of ZnT3-dependent zinc in contrast gain control and that ZX1 does not have any non-ZnT3-dependent effects on contrast gain control. In littermate controls, ZnT3-WT mice, ZX1 treatment caused a reduction in the contrast scaling factor (Fig. 4t; p = 4.30e-4, permutation test; n = 48 cells from four mice), which was not different from the reduction we observed in Figure 4o. Together, these results suggest that ZnT3-dependent synaptic zinc is needed for contrast gain control in principal neurons of mouse L2/3 A1.

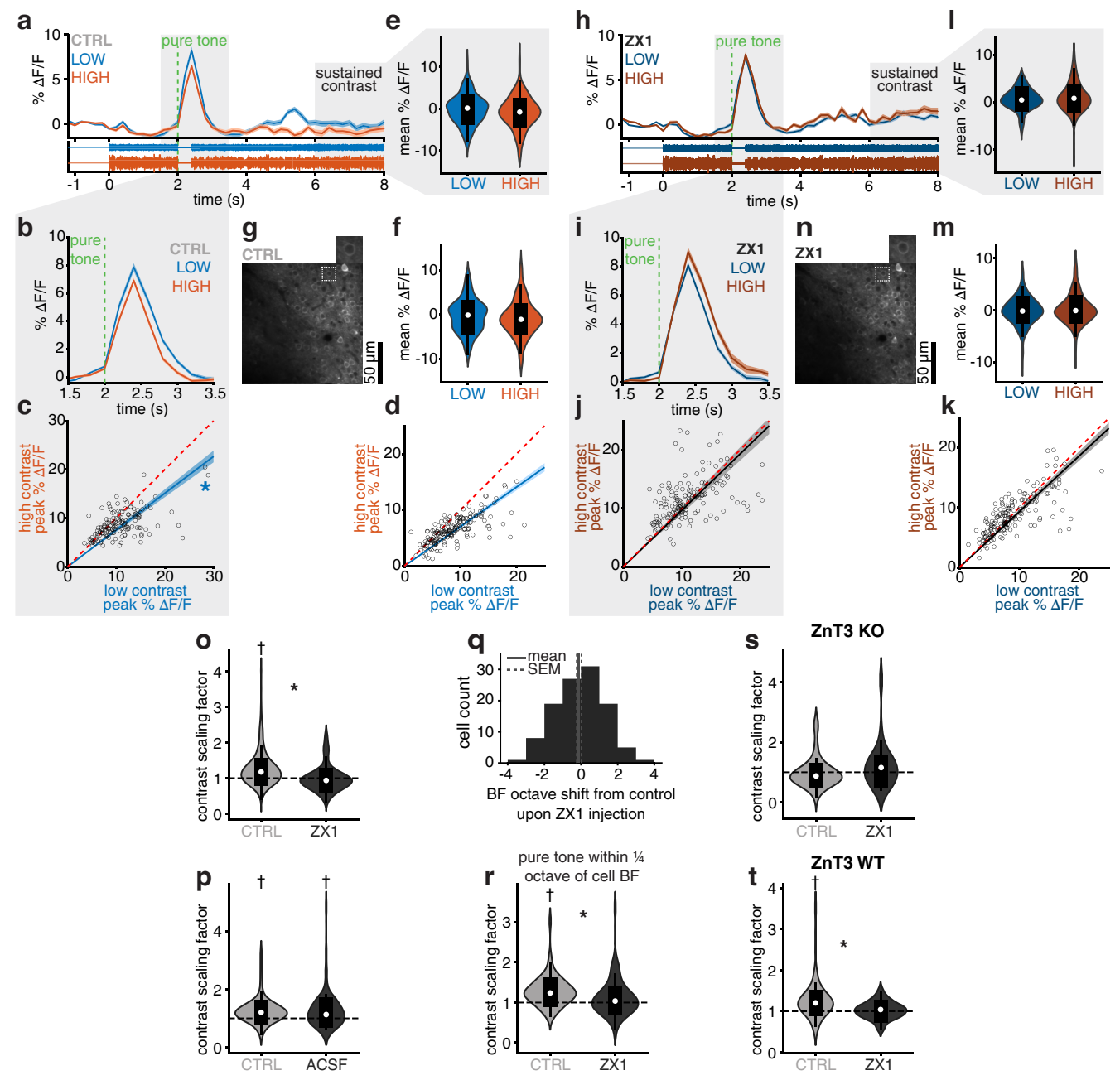


Figure 4. Contrast gain control in A1 principal cells depends on cortical ZnT3-dependent synaptic zinc signaling. *a*, Mean ± SEM of % ΔF/F traces from A1 principal cells before ZX1 treatment (CTRL) during low (blue) and high (orange) contrast stimuli with a 400 ms pure tone occurring 2 s after the initiation of the DRC stimulus. Baseline, F₀, for % Δ F/F calculated before DRC onset at -1.2 to 0 s. Bottom, Representative sound voltage signals. b, Left, Mean \pm SEM of % Δ F/F traces during the pure tone epoch during CTRL treatment calculated as $F(t) - F_0$ using F (t) in \boldsymbol{a} and F_0 as F(t) at 1-2 s. \boldsymbol{c} , Scatterplots of each cell's mean peak % $\triangle F/F$ pure tone response in low versus high contrast during CTRL treatment. In scatterplot, significance (p = 9.99e-6, permutation test) denoted by blue asterisk (*) and direction of contrast effect denoted by blue coloring of fitted regression line and 95% CI (slope 95% CI: 0.71-0.80). d, Same as in c, but without trace selection (p = 10.00e-6, permutation test, regression slope 95% Cl: 0.67-0.73, n = 179 cells from 9 mice). e, Violin plot of temporal averages of % Δ F/F responses during the sustained contrast epoch at 6-8 s during CTRL treatment for low (blue) and high (orange) contrast (p = 8.87e-2, permutation test). White dot represents median. Thick black line indicates interguartile range. Contour lines indicate data distribution. f_s Same as in e_s but without trace selection (p = 2.48e-01, permutation test, n = 179 cells from 9 mice). g_s Representative 2-photon image of A1 L2/3 CaMKII expressing principal neurons during CTRL treatment. h-n, Same as in a-q, but after ZX1 treatment. j, Scatterplot: p = 2.67e-1, permutation test; slope 95% Cl: 0.91-1.02. **k**, Same as in **j**, but without trace selection (p = 8.74e-01, slope 95% Cl: 0.89-0.97, n = 179 cells from 9 mice). **I**, Violin plot: p = 1.45e-1, permutation test. **m**, Same as in **I**, but without trace selection (p = 1.782582e-01, permutation test, n = 179 cells from 9 mice). **o**, Contrast scaling factors before (CTRL; light gray) and after (dark gray) ZX1 treatment (p = 9.99e-6, permutation test, n = 179 cells from 9 mice). tion test). CTRL contrast scaling factors significantly >1 (p=1.12e-10) and ZX1 contrast scaling factors not significantly different from 1 (p=5.03e-2, Wilcoxon signed-rank tests). **a-c**, **e**, **h-j**, o, N = 150 cells from 9 mice. p, Same as in o, but before and after ACSF treatment (N = 73 cells from 6 mice; CTRL vs ACSF: p = 9.49e-1, permutation test). CTRL and ACSF treatments significantly >1 (p=9.53e-8, p=1.61e-4, Wilcoxon signed-rank tests). **q**. Histogram representing cell counts for bins of cell BF octave shifts after ZX1 treatment. **r**, Same as in **i**, but limited to responses from pure tones occurring within 0.25 octave of cell BF calculated from FRAs both before and after ZX1 treatment (N = 69 cells from 5 mice; CTRL vs ZX1: p = 3.41e-2, permutation test; CTRL significantly >1, p=4.89e-8 Wilcoxon signed-rank test). s, t, Same as in I, but in ZnT3-K0 (s, N=61 cells from 4 mice; CTRL vs ZX1: p=8.66e-2, permutation test) and ZnT3-WT mice (t, N = 48 cells from 4 mice; CTRL vs ZX1: p = 4.30e-4; CTRL significantly >1, p = 1.24e-5, Wilcoxon signed-rank test). *p < 0.05 (permutation test). †p < 0.001 (Wilcoxon signed-rank test).

Zinc signaling does not have any contrast-dependent effects on either PV or SOM cells

Because zinc signaling affects the sound-evoked responses of PV and SOM interneurons (Anderson et al., 2017), we next explored whether zinc signaling affects potential contrast adaptations in these interneurons. To do so, we performed the same assay as in Figure 1i, but in PV (n = 43 cells from 6 mice) and SOM cells (n = 20 cells from 6 mice) before and after injection of ZX1 into ACtx. To target GCaMP6f expression to PV or SOM cells, we injected the ACtx of mice expressing Cre recombinase in PV or SOM cells, PV- or SOM-Cre mice, with a Cre-dependent GCaMP6f AAV. In both PV and SOM cells, we did not observe any significant contrast-dependent effect before or after ZX1 injection, suggesting that the A1 PV and SOM cell populations do not contribute to contrast adaptation of L2/3 A1 principal neurons (Fig. 5; p > 0.05 in scatter plots and violin plots, permutation test). Although the numbers of animals used for the PV and SOM experiments were comparable with those of the principal neuron experiment cohorts, there are fewer interneuron cells in the 2PCI FOV than principal cells, thus leading to lower sample sizes compared with principal cells. It is possible that this smaller number of cells rendered our analysis underpowered to detect contrast-dependent effects. Nonetheless, these results are consistent with previous findings regarding the lack of a role of PV cells in sound contrast adaptation (Cooke et al., 2020) and further suggest that zinc signaling does not have any contrast-dependent effects in SOM cells.

Zinc signaling suppresses principal neuron responses preceded by high, but not low, sound level contrast

Despite the population effect of decreased pure tone response amplitude following high contrast, our results reveal heterogeneity in scaling: we observed cells that did not show contrast effects and others that showed increased pure tone responses following high contrast (Figs. 1e,k,r,s, 4c,d). To assess whether the ZX1 effect is consistent across this heterogeneous population, we apportioned cells into top, middle, and bottom third percentiles based on the magnitude of their contrast scaling factors in CTRL (Fig. 6a; 50 cells in each condition from a total of 150 cells from 9 mice). ZX1 caused a significant decrease in the average contrast scaling factor in the top and middle percentiles (Fig. 6a; p = 9.99e-6 and p = 3.60e-2, respectively, permutation tests), but did not change the average contrast scaling factor in the bottom third percentile (Fig. 6a; p = 9.31e-2, permutation test). In the top third percentile, all 50 cells showed contrast scaling factors >1 in CTRL (contrast gain control) and ZX1 decreased contrast scaling factors in 49 cells. In the middle third, percentile all 50 cells showed contrast scaling factors >1 in CTRL and ZX1 decreased contrast scaling factors in 40 cells. In the bottom third percentile, 7 of 50 cells showed contrast scaling factors >1 in CTRL and in 5 of these 7 cells ZX1 decreased contrast scaling factors. In the bottom third percentile, 43 of 50 that showed contrast scaling factors <1 in CTRL, and ZX1 decreased contrast scaling factors in 21 of these 43 cells. Overall, because ZX1 solely had a significant effect on those cells exhibiting contrast gain control (contrast scaling factors >1), and did not significantly affect the population of cells with contrast scaling factors significantly <1, these results suggest that the effect of ZX1 is specific to those cells showing contrast gain control in CTRL.

We next asked whether the effect of zinc signaling is limited to responses following low or high contrast, or both. To

address this, we plotted peak pure tone response amplitude across the principal cell population following low- and highcontrast DRCs before and after ZX1 injection (Fig. 6b-d; n = 150 cells from 9 mice). Using a repeated-measures twoway ANOVA, we compared the effect of the contrast and ZX1 factors on peak % Δ F/F responses. We observed significant main effects of both contrast $(F_{(1,149)} = 32.07, p = 7.44e$ 8) and ZX1 ($F_{(1,149)} = 10.41$, p = 1.54e-3) with a significant interaction effect between the two $(F_{(1,149)} = 31.75, p = 8.51e-8)$. Bonferroni-corrected post hoc tests for multiple comparisons revealed that peak response amplitudes were significantly lower in high- compared with low-contrast before (Fig. 6b; p = 7.16e-15) but not after ZX1 injection (Fig. 6*b*; p = 0.3543). Importantly, ZX1 increased peak response amplitudes in high contrast (Fig. 6b; p = 2.54e-10), but left amplitudes unaffected in low contrast (Fig. 6*b*; p = 0.1325). Scatterplots of peak pure tone responses before versus after ZX1 following low (Fig. 6c) or high (Fig. 6d) contrast showed that ZX1 did not affect peak responses in low contrast (Fig. 6c; p = 4.67e-1, permutation test; slope 95% CI: 0.88-1.01) but increased peak responses in high contrast (Fig. 6d; p = 9.99e-6, permutation test; slope 95% CI: 1.16-1.31). To control for a potential effect of the injection pipette and the injection of a solution volume in cortex, we performed the same analysis before and after ACSF injection (Fig. 6e; n = 73 cells from 6 mice). We solely observed a significant main effect of contrast $(F_{(1,72)} = 42.05, p = 9.71e-9)$ and no significant interaction effect between contrast and ACSF injection. Scatterplots of peak pure tone responses before versus after ACSF injection following low (Fig. 6f) or high contrast (Fig. 6g) showed that ACSF did not affect peak responses in either condition (p > 0.05, permutation tests). Together, these results suggest that zinc signaling suppresses pure tone responses specifically in high-contrast, but not low-contrast, sound.

Discussion

2PCI assay for contrast adaptation: strengths and limitations

To assess contrast gain control mechanisms, we used a 2PCI preparation to measure pure tone scaling by preceding contrast. This approach of assessing contrast gain control is based on an experiment in a seminal study using electrophysiology in ferret A1 reporting that responses to fixed test sounds within neurons' receptive fields are scaled by spectrotemporal contrast of a preceding sound context (Rabinowitz et al., 2011). Similarly, a more recent study from the same group revealed that, in single cells of mouse A1, sound-evoked excitatory postsynaptic potentials decrease when preceded by high-contrast sound (Cooke et al., 2020). A calcium imaging approach allows for a large range of spatial scales, thus enabling facile parcellation of auditory fields by tonotopy and anatomy on the mesoscale for A1 localization, as well as single-cell resolution with cell-type specificity, via viral and transgenic targeting. These advantages come at the cost of temporal resolution. While the signal decay of the GCaMP6f calcium indicator (\sim 1 s for one action potential) (T. W. Chen et al., 2013) may be resolved with spike deconvolution (Pachitariu et al., 2017), our recordings are still limited by a 5 Hz imaging frame rate because of X-Y galvanometric laser scanning at 256×256 pixels. These constraints preclude the estimation of temporal kernels and accurate contrast adaptation time constants. We observed an effect of contrast on pure tone responses with a longer time scale than previously reported, >500 ms versus 86-157 ms (median adaptation times in Rabinowitz et al., 2011). This discrepancy may be attributable to calcium signal

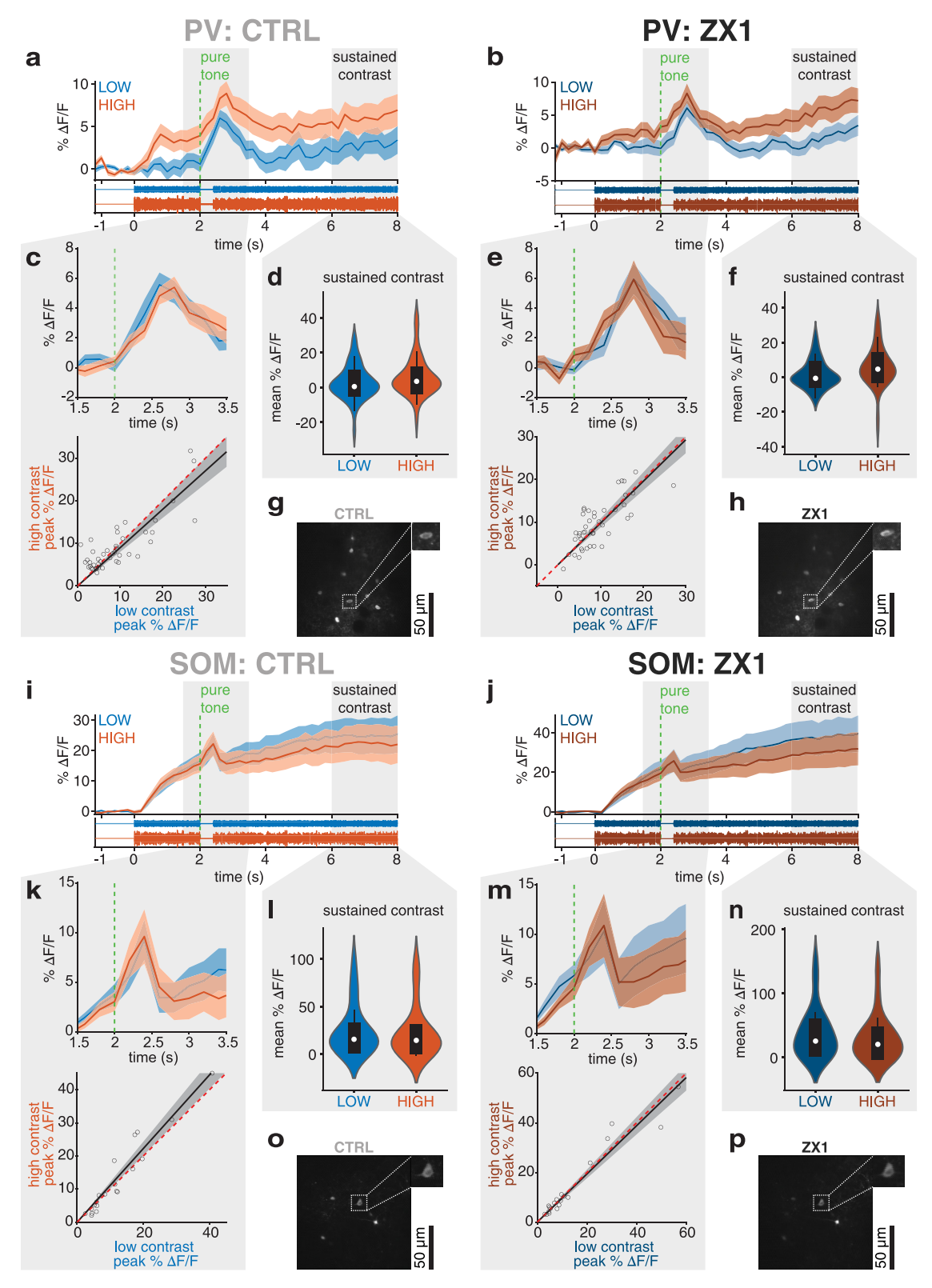


Figure 5. Zinc signaling does not have any contrast-dependent effects on either A1 PV or SOM cells. \it{a} , \it{b} , Mean \pm SEM of % Δ F/F traces from PV cells before (\it{a}) and after ZX1 treatment (\it{b}) during low (blue) and high (orange) contrast stimuli with a 400 ms pure tone occurring at 2 s. Baseline, F₀, for % Δ F/F calculated before DRC onset at -1.2 to 0 s. Bottom, Representative sound voltage signals. \it{c} , \it{e} , Top, Mean \pm SEM of % Δ F/F traces from PV cells during the pure tone epoch before (\it{c} , top) and after (\it{e} , top) ZX1 treatment calculated as F(t) - F₀ using F(t) in \it{a} , \it{b} and F₀ as F(t) at 1-2 s. \it{c} , \it{e} , Bottom, Scatterplot of each PV cell's mean peak % Δ F/F pure tone response in low versus high contrast before (\it{c} , bottom; \it{p} = 7.91e-1, permutation test; slope 95% Cl: 0.87-1.08) ZX1 treatment (\it{N} = 43 cells from 6 mice). \it{d} , \it{f} , Violin plot of temporal averages of % Δ F/F responses from PV cells during the sustained contrast epoch at 6-8 s before (\it{d} , \it{p} = 1.55e-1, permutation test) and after ZX1 treatment (\it{f} , \it{p} = 5.14e-2, permutation test) for low (blue) and high (orange) contrast. White dot represents median. Thick black line indicates interquartile range. Contour lines indicate data distribution. \it{g} , \it{h} , Representative 2-photon image of A1 L2/3 PV neurons before (\it{g}) and after (\it{h}) ZX1 treatment. $\it{i-p}$, Same as in $\it{a-h}$, but recorded in SOM cells (\it{N} = 20 cells from 6 mice). \it{k} , \it{m} , Bottom, CTRL: \it{p} = 7.85e-1, permutation test, slope 95% Cl:

decay from the DRC sound onset obscuring responses from earlier occurring pure tones.

Millisecond temporal resolution, as afforded by electrophysiology, allows for the simultaneous estimation of separable frequency and temporal kernels (Linden et al., 2003; Ahrens et al., 2008), as well as spectrotemporal contrast kernels, to evaluate temporal and spectral regions within which a neuron is most sensitive to contrast changes (Rabinowitz et al., 2012). Our frame acquisition interval (200 ms) exceeds the reported temporal bandwidths of A1 neurons (Linden et al., 2003; Lohse et al., 2020), and thus precludes temporal kernel estimation. Assessing spectral contrast kernels with our 2PCI assay would require a separate stimulus trial for which contrast is low or high at individual frequency bins along the DRC bandwidth. For a given experiment, this would require a prohibitive number of trial repetitions for a sufficient frequency bin resolution. Thus, the analysis of frequency dependence in Figure 3 does not directly compare to spectral contrast kernels (Rabinowitz et al., 2012). Cell spectral contrast kernels correlate with cell frequency kernels; cells are most sensitive to changes in contrast, and thus show greater contrast gain control, along the frequency region at which they are most responsive (Rabinowitz et al., 2012). Here, because contrast extends across the full DRC bandwidth, we would expect to capture comparable contrast gain control among cells with different FRAs. Given this, our finding that contrast gain control is comparable between pure tone stimulus frequencies both near and away cell BFs (Fig. 3d) is consistent with previous studies (Rabinowitz et al., 2012). Our results thus consider the frequency dependence between cell tuning and contrast effects on pure tone responses, rather than frequency regions of the contrast bandwidth.

Heterogeneity in scaling: inclusion criteria, recording depth, and contrast tuning

Despite the population effect of decreased pure tone response amplitude following high contrast, our results reveal heterogeneity in scaling: we observed cells that did not show contrast effects and others that showed increased pure tone response amplitude following high contrast (Figs. 1e,k,r,s, 4c,d). This may be attributable to several factors, such as inclusion criteria, recording depth (Cooke et al., 2018), and potential tuning to contrast (Barbour and Wang, 2003). Previous studies that measured contrast gain control with either multiunit (Rabinowitz et al., 2011; Cooke et al., 2018, 2020) or single-unit recordings (Rabinowitz et al., 2012; Lohse et al., 2020) included units based on reliable firing-rate responses to the DRC stimuli (Rabinowitz et al., 2012). Moreover, a greater proportion of cells would exhibit contrast gain control had we extended our imaging plane below L2/3, because of increases in the magnitude of contrast gain control in deeper cortical layers (Cooke et al., 2018). Furthermore, if the contrast tuning that is observed in marmoset ACtx (Barbour and Wang, 2003) extends to mouse ACtx, variability could also be explained by tuning to spectral contrast level, albeit not spectrotemporal. Additional experiments are needed to determine the presence of contrast tuning in mouse ACtx and whether variability is captured by auditory subfield-dependent differences (Barbour and Wang, 2003).

←

1.01-1.22; ZX1: p = 9.98e-1, permutation test, slope 95% Cl: 0.88-1.06. **I**, **n**, CTRL: p = 7.51e-1, ZX1: p = 5.26e-1, permutation tests. Black/gray coloring of regression lines and 95% Cls represent no significant effect of contrast (permutation tests). **o**, **p**, Representative 2-photon image of A1 L2/3 SOM neurons before (**o**) and after (**p**) ZX1 treatment.

DRC stimulus: robustness and comparison with prior studies

Contrast gain control in mouse ACx is reliably elicited despite sound level and frequency differences in contrast DRC stimuli. Prior studies observed contrast gain control using DRC stimuli with average sound levels of 40 dB (Cooke et al., 2020; Lohse et al., 2020) and 80 dB (Cooke et al., 2018), both with a doubling of sound level range at high contrast (low Δ dB: 20, high Δ dB: 40). Our DRC stimuli are defined by a 55 dB mean, a tripling of sound level range from 10 dB in low to 30 dB in high, and narrower bandwidths, 5-52 or 5-25 kHz compared with 1-64 kHz, with narrower frequency intervals, 1/8th and 1/12th octave, respectively, versus 1/4th octave. Despite these differences, we observed significant response scaling by contrast (Fig. 1r,s), further confirming the robustness of cortical contrast gain control.

Different cellular and neuromodulatory mechanisms underlie cortical contrast gain control and contrast invariance

Synaptic zinc solely affected contrast gain control in principal neurons, while leaving contrast invariance unaffected (Fig. 4). Consistent with this, and with recent findings negating inhibitory interneuron involvement in contrast gain control (Cooke et al., 2020), we observed no effect of contrast in either PV or SOM interneurons, nor a contrast-dependent effect of zinc (Fig. 5). Although sustained PV responses to high contrast DRC appear larger than those in low contrast, the effect of contrast was not significant. This motivates further investigation with larger sample sizes and subpopulation specificity within the PV and SOM populations (Harris and Shepherd, 2015; Anirban et al., 2017). Nonetheless, our findings support that the two phenomena of contrast adaptation occur via separate mechanisms.

Zinc signaling and cell spectrotemporal receptive fields (STRFs)

Although we addressed the spectral tuning effects of ZX1 (Fig. 4q,r), we were unable to estimate temporal kernels and thus complete STRFs because of the temporal resolution constraints of our calcium imaging acquisition rate (5 Hz). This precluded an analysis of potential zinc effects on temporal tuning. Rabinowitz et al. (2012) reported that units are most sensitive to contrast within 50-100 ms of recent stimulation. In that study, the linear STRF, including the separable temporal kernel, is used for calculating the contrast kernel parameters of the nonlinear input-output model. Thus, a change in temporal tuning could be pursuant to changes in temporal contrast tuning (Rabinowitz et al., 2012). However, given that the 2 s contrast context of our stimulus paradigm well exceeds both the temporal contrast kernel window and temporal bandwidth of A1 neurons, we would consider temporal tuning effects to be negligible using our 2PCI assay. Nonetheless, STRF estimations via cortical recordings with millisecond temporal resolution would provide a clearer picture of zinc's cell-specific effects on spectrotemporal tuning.

Stimulus- and context-dependent effects of zinc signaling in cortical sound processing

Our results support that synaptic zinc signaling is necessary for contrast gain control in A1. The reported intracortical diffusion area of ZX1 is $2.1 \pm 0.1 \text{ mm}^2$, which was based on visualizing the spread of the extracellular red fluorescent dye Alexa-594, coinfused with ZX1 (Anderson et al., 2017). When this diffusion area is converted to radius $(0.8 \pm 0.2 \text{ mm})$, it suggests that the spread of ZX1 is limited exclusively to cortex (Lein et al., 2007), assuming that ZX1 spreads similarly to Alexa-594. The fact that this

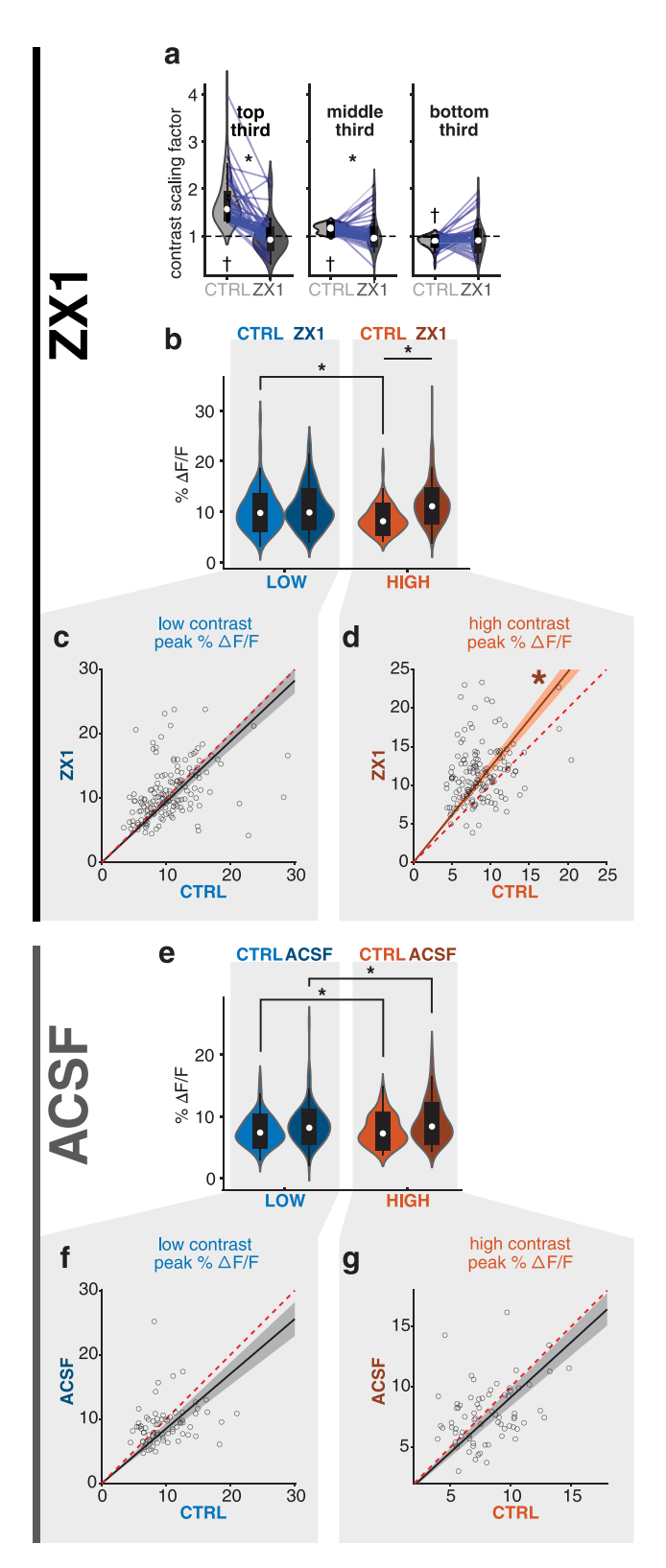


Figure 6. Zinc signaling suppresses A1 pure tone responses preceded by high, but not low, sound level contrast. a, Violin plots of contrast scaling factor of cells in top (N=50 cells), middle (N=50 cells), and bottom (N=50 cells) third percentiles in CTRL, shown during CTRL (light gray) and ZX1 (dark gray) treatment. White dot represents median. Thick black line indicates interquartile range. Contour lines indicate data distribution. Top third percentile: CTRL versus ZX1: p=9.99e-6, permutation test; CTRL significantly >1, p=7.56e-10, Wilcoxon signed-rank test. Middle third percentile: CTRL versus ZX1: p=3.60e-2, permutation test; CTRL significantly >1, p=7.56e-10, Wilcoxon signed-rank test. Bottom third percentile: CTRL versus ZX1: p=1.41e-1, permutation test; CTRL significantly <1, p=1.20e-8,

cortical zinc chelation eliminates contrast gain control in A1 supports that A1 sound contrast gain control is likely not simply inherited from the thalamus; but importantly, even if inherited, it depends on cortical zinc for its implementation.

Zinc signaling decreases pure tone response amplitudes in principal cells, specifically when they are preceded by high-contrast DRC stimuli (Fig. 6b,d). However, zinc signaling has no effect on pure tones preceded by low contrast (Fig. 6b,c). These results suggest a context-dependent effect of zinc signaling on cortical sound processing, likely because of context (experience)dependent changes in synaptic zinc signaling. Sensory processing centers that express synaptic zinc (ZnT3) exhibit experience-dependent changes in vesicular zinc labeling, suggesting that the effects of synaptic zinc signaling are activity-dependent (Brown and Dyck, 2002, 2005; Nakashima and Dyck, 2009). Indeed, we previously showed that synaptic zinc levels in the dorsal cochlear nucleus (DCN) are decreased following exposure to loud sound, and thus modulate glutamatergic neurotransmission in an experience-dependent manner (Kalappa et al., 2015; Vogler et al., 2020). Importantly, synaptic zinc is a context-dependent modulator of short-term plasticity in DCN synapses: at lower levels of activity, synaptic zinc reduces EPSC responses, but at higher levels, it inhibits responses during the first few stimuli, while enhancing responses during subsequent stimuli (Kalappa and Tzounopoulos, 2017). At the receptor level, zinc inhibits NMDARs in a subunitspecific manner with affinities ranging from nanomolar to high micromolar. Finally, multiple receptors that can be inhibited by zinc can also be potentiated by zinc at either lower (e.g., glycine receptors, AMPAR, GluK3 kainate receptors, and P2X2-4R purinergic receptors) or higher (e.g., GABAAR) concentrations of the metal. Together, these studies and the results presented here highlight that the effects of synaptic zinc signaling on neurotransmission, neurotransmitter receptors, and sound-evoked cortical responses are zinc concentration-, receptor-, subunit-, stimulus-, context-, and activitydependent.

Within this context, the zinc signaling effects on pure tone response amplitude shown here do not simply compare with our previous work (Anderson et al., 2017). For example, we previously showed that zinc signaling increases the response amplitude to 12 kHz pure tones in principal cells (Anderson et al., 2017), whereas here we show that zinc signaling decreases pure tone response amplitudes in high-contrast sound. Similarly, with

←

Wilcoxon signed-rank test. $\uparrow p < 0.05$, contrast scaling factors that are significantly different from 1 (Wilcoxon signed-rank test). **b**. Violin plot of principal cell peak pure tone $\% \Delta F/F$ responses preceded by 2 s of low (blue) and high (orange) sound level contrast before (light shade; CTRL) and after (dark shade) ZX1 treatment (repeated-measures ANOVA: intercept: $F_{(1,149)} = 2118.8$, p = 5.49e-90; contrast: $F_{(1,149)} = 32.07$, p = 7.44e-8; ZX1: $F_{(1,149)} = 10.41$, p = 1.54e-3; interaction: $F_{(1,149)} = 31.75$, p = 8.51e-8; CTRL: low vs high: p = 7.16e-15; high contrast CTRL vs ZX1: p = 2.54e-10). **c**, **d**, Scatterplot of each cell's mean peak % Δ F/F pure tone response before (CTRL, x axis, light shade) versus after (y axis, dark shade) ZX1 treatment in low (\mathbf{c}) and high (\mathbf{d}) contrast (N = 150 cells from 9 mice). Black/gray coloring of regression line and 95% CI (on c) represent no significant effect of ZX1 treatment (p = 4.67e-1, permutation test; slope 95% CI: 0.88-1.01). Significant ZX1 effect (p = 9.99e-6, permutation test; slope 95% CI: 0.88-1.01)permutation test) in **d** denoted by dark red asterisk (*) and fitted regression line with 95% CI (slope 95% CI: 1.16-1.31). **e-g**, Same as in **b-d**, but with ACSF treatment instead of ZX1 (N = 73 cells from 6 mice; repeated-measures ANOVA: intercept: $F_{(1.72)} = 1278.5$, p = 1.41e47; contrast: $F_{(1.72)} = 42.05$, p = 9.71e-9; ACSF: $F_{(1.72)} = 2.62$, p = 1.10e-1; interaction: $F_{(1.72)} = 0.421$, p = 5.19e-1; CTRL: low vs high: p = 1.83e-06; ACSF: low vs high: p = 8.98e-164). Black/gray coloring of regression lines and 95% Cls (on **f**, **g**) represent no significant effect of ACSF treatment (low contrast: p = 2.29e-1, permutation test, slope 95% CI: 0.76-0.94; high contrast: p = 4.66e-1, permutation test, slope 95% CI: 0.84-0.99). **b**, **e**, *p < 0.001, significant Bonferroni-corrected post hoc comparisons.

Table 1. Statistical analysis without any trace selection

Figure	р	Statistical test	N (cells)	N (mice)
1r	p = 10.00e-6	Permutation	152	8
1s	p = 10.00e-6	Permutation	122	7
1t, 5-25 vs 5-52 scale factor	p = 10.00e-6	Permutation	152 vs 122	8 vs 7
1t, 5-25 scaling factor	p = 2.71e-18	Wilcoxon signed rank	152	8
1t, 5-52 scaling factor	p = 2.60e-17	Wilcoxon signed rank	122	7
1u, 5-25 invariance	p = 9.51e-01	Permutation	152	8
1v, 5-52 invariance	p = 4.44e-01	Permutation	122	7
2 <i>c</i>	p = 153e-01	Permutation	228	15
3 <i>b</i>	p = 10.00e-06	Permutation	161	15
36	p = 10.00e-06	Permutation	113	15
3d, within vs outside	p = 2.18e-01	Permutation	161 vs 113	15
3d, within scaling factor	p = 2.76e-21	Wilcoxon signed rank	161	15 15
3d, outside scaling factor	p = 1.07e-14	Wilcoxon signed rank	113	9
4o, control scaling factor	p = 10.00e-06	Permutation test	179 179	9
40, control scaling factor	p = 8.64e-23 p = 3.52e-01	Wilcoxon signed rank	179	9
4o, ZX1 scaling factor 4p, control vs ACSF	p = 3.32e-01 p = 8.96e-01	Wilcoxon signed rank Permutation	94	6
4p, control scaling factor	p = 0.90e-0.1 p = 1.33e-12	Wilcoxon signed rank	94	6
4p, ACSF scaling factor	$p = 1.53e^{-12}$ $p = 8.60e^{-09}$	Wilcoxon signed rank	94	6
4r, control vs ZX1	p = 0.00e-09 p = 10.00e-06	Permutation	69	5
4r, control scaling factor	p = 6.50e-13	Wilcoxon signed rank	69	5
4r, ZX1 scaling factor	p = 0.300 TS p = 8.21e-01	Wilcoxon signed rank	69	5
4s, control vs ZX1	p = 6.20e-01	Permutation	61	4
4s, control scaling factor	p = 0.200 or $p = 1.67 e - 0.1$	Wilcoxon signed rank	61	4
4s, ZX1 scaling factor	p = 1.00e-01	Wilcoxon signed rank	61	4
4t, control vs ZX1	p = 10.00e-06	Permutation	48	4
4t, control scaling factor	p = 1.02e-07	Wilcoxon signed rank	48	4
4t, ZX1 scaling factor	p = 5.00e-02	Wilcoxon signed rank	48	4
5c, scatter plot	p = 9.55e-01	Permutation	45	6
5d, violin plot	p = 1.50e-01	Permutation	45	6
5e, scatter plot	p = 4.67e-01	Permutation	45	6
5f, violin plot	p = 8.93e-02	Permutation	45	6
5k, scatter plot	p = 7.80e-01	Permutation	20	6
5i, violin plot	p = 7.47e-01	Permutation	20	6
5m, scatter plot	p = 9.99e-01	Permutation	20	6
5n, violin plot	p = 5.60e-01	Permutation	20	6
6a, top third, control vs ZX1	p = 10.00e-06	Permutation	60	9
6a, top third, control scaling factor	p = 1.63e-11	Wilcoxon signed rank	60	9
6a, top third, Zx1 scaling factor	p = 3.00e-1	Wilcoxon signed rank	60	9
6a, middle third, control vs ZX1	p = 10.00e-06	Permutation	59	9
6a, middle third, control scaling factor	p = 2.39e-11	Wilcoxon signed rank	59	9
6a, middle third, ZX1 scaling factor	p = 9.80e-1	Wilcoxon signed rank	59	9
6a, bottom third, control vs ZX1	p = 8.24e-02	Permutation	60	9
6a, bottom third, control scaling factor	p = 7.01e-1	Wilcoxon signed rank	60	9
6a, bottom third, ZX1 scaling factor	p = 5.00e-03	Wilcoxon signed rank	60	9
6b, control low vs high	p = 1.85e-21	Bonferroni correction	179	9
6b, ZX1 low vs high	p = 9.13e-1	Bonferroni correction	179	9
6b, high, control vs ZX1	p = 3.51e-22	Bonferroni correction	179	9
6b, low, control vs ZX1	p = 7.56e-1	Bonferroni correction	179	9
6b, contrast effect	p = 4.56e-8	Repeated-measures two-way ANOVA	179	9
6b, ZX1 effect	p = 6.27e-11	Repeated-measures two-way ANOVA	179	9
6b, interaction effect	p = 3.12e-17	Repeated-measures two-way ANOVA	179	9 9
6c	p = 9.48e-01	Permutation	179 170	9
6d 6e, control, low vs high	p = 10.00e-06	Permutation Bonferroni correction	179 94	6
6e, ACSF, low vs high	p = 2.35-23 p = 4.58e-14	Bonferroni correction Bonferroni correction	94 94	0
6e, high, control vs ACSF	p = 4.58e-14 p = 7.03e-2	Bonferroni correction Bonferroni correction	94 94	0 6
6e, low, control vs ACSF	p = 7.03e-2 p = 1.79e-1	Bonferroni correction	94 94	6
6e, contrast effect	p = 1.79e-1 p = 3.30e-24	Repeated-measures two-way ANOVA	94	6
6e, ACSF effect	p = 3.30e-24 p = 9.30e-02	Repeated-measures two-way ANOVA	94	6
6e, interaction effect	p = 7.27e-1	Repeated-measures two-way ANOVA	94	6
6f	$p = 7.27e^{-1}$ p = 2.88e-01	Permutation	94	6
6 <i>g</i>	p = 3.50e-01	Permutation	94	6

regard to PV and SOM cells, we previously showed that zinc signaling decreases pure tone response amplitude (Anderson et al., 2017), whereas here we show that zinc signaling does not affect pure tone response amplitude in either PV or SOM cells (Fig. 5c, e,k,m). The 12 kHz 0.5 s pure tones we used previously were preceded by silence (Anderson et al., 2017), whereas the pure tones used here were preceded by low- or high-contrast DRC stimuli lasting 0.5-2 s and consisting of a summation of 28-29 pure tone frequencies at varying sound level intensities. It is likely that the preceding sound context of low- or high-contrast DRC elicits activity-dependent changes in zinc signaling, including changes in the main targets of zinc signaling, such glutamatergic and GABAergic neurotransmission (Anderson et al., 2015; Kalappa et al., 2015; Kouvaros et al., 2020), or changes in zinc release (Vogler et al., 2020). For example, pharmacological blockade of glutamate NMDARs changes the effect of zinc signaling on the amplitude of sound-evoked responses in cortical principal neurons from excitatory to inhibitory (Anderson et al., 2017). Thus, it is possible that the inhibitory effect of zinc signaling on principal cell pure tone response amplitude in high contrast is attributable to differential NMDAR engagement during high- versus low-contrast DRC stimuli. Thus, the ostensible incongruities of zinc signaling between this study and our previous ones are likely foremost explained by activity-dependent changes in zinc signaling induced by differences in the context within which the pure tone stimulus is delivered.

Regarding responses to the DRC sound onset, the lack of zinc effects on responses to the DRC sound onset compared with previously published effects zinc effects on pure tone stimuli (Anderson et al., 2017) may similarly be explained by stimulusdependent changes in zinc signaling. The DRC stimulus persists for much longer than the isolated 12 kHz pure tone stimulus used in previous studies (Anderson et al., 2017), includes multiple frequencies, and thus allows for adaptation and recruitment of a broader population of neurons and neural response properties. Finally, the effect of zinc signaling on pure tone responses is sound level-dependent. In principal neurons, responses to pure tones at dB <70 are not affected by zinc signaling (Anderson et al., 2017). Here, the sound level of the DRC stimulus varies around a 55 dB mean at 25 ms intervals. Thus, the lack of a zinc signaling effect on responses to DRC sound onset is likely because of stimulus- and context-dependent effects of zinc signaling.

In our previous studies (Kumar et al., 2019), we found that the effect of zinc signaling on pure tone responses in principal cells depends on the octave distance between the pure tone stimulus and the cell's BF. Namely, zinc signaling increases pure tone response amplitude when tone frequencies are near cell BF but decreases pure tone response amplitude when tone frequencies are away from cell BF. The low- and high-contrast DRC stimuli that preceded our pure tone stimuli consisted of a summation of 28-29 pure tone frequencies, both near to and away from cell BFs. Thus, one explanation for the observed inhibitory effect of zinc signaling in pure tone response amplitude in high contrast is that the effects of frequencies in the DRC that are away from cell BF may continue through to the pure tone onset and thus may influence cell responses to the pure tone stimulus. The highcontrast dependence of this effect could be explained by the greater sound level deviations between frequencies in high contrast compared with low contrast (Fig. 1b). Together, stimulus differences of context, frequency, level, and duration preclude a 1:1 comparison with our prior studies but highlight the stimulusand context-dependent effects of zinc signaling in cortical sound processing.

The importance of zinc signaling in neurotransmission and in cortical sensory processing is unequivocal (McAllister and Dyck, 2017b; Krall et al., 2021). However, since the effects of zinc at the molecular, cellular, circuit, and systems levels are highly complex, they are not easily integrated into one simple picture yet. Indeed, this points to the need for further rigorous investigations on the various roles and mechanisms of stimulus- and context-dependent zinc signaling on cortical processing. In future studies, this will be aided by the use of mouse lines that enable conditional KO of synaptic zinc signaling in specific cortical cell types, as well as genetically encoded zinc fluorescent sensors localized at the synapse.

References

- Ahrens MB, Linden JF, Sahani M (2008) Nonlinearities and contextual influences in auditory cortical responses modeled with multilinear spectrotemporal methods. J Neurosci 28:1929–1942.
- Anderson CT, Radford RJ, Zastrow ML, Zhang DY, Apfel UP, Lippard SJ, Tzounopoulos T (2015) Modulation of extrasynaptic NMDA receptors by synaptic and tonic zinc. Proc Natl Acad Sci USA 112:E2705–E2714.
- Anderson CT, Kumar M, Xiong S, Tzounopoulos T (2017) Cell-specific gain modulation by synaptically released zinc in cortical circuits of audition. Elife 6:e29893.
- Angeloni CF, Mlynarski W, Piasini E, Williams AM, Wood KC, Garami L, Hermundstad A, Geffen MN (2021) Cortical efficient coding dynamics shape behavioral performance. bioRxiv 455845. doi: 10.1101/2021.08.11. 455845.
- Anirban P, Crow M, Raudales R, He M, Gillis J, Huang ZJ (2017) Transcriptional architecture of synaptic communication delineates GABAergic neuron identity. Cell 171:522–539.e20.
- Barbour DL, Wang X (2003) Contrast tuning in auditory cortex. Science 299:1073–1075.
- Brown CE, Dyck RH (2005) Modulation of synaptic zinc in barrel cortex by whisker stimulation. Neuroscience 134:355–359.
- Brown CE, Dyck RH (2002) Rapid, experience-dependent changes in levels of synaptic zinc in primary somatosensory cortex of the adult mouse. J Neurosci 22:2617–2625.
- Carandini M, Heeger DJ (2011) Normalization as a canonical neural computation. Nat Rev Neurosci 13:51–62.
- Chen Q, Deister CA, Gao X, Guo B, Lynn-Jones T, Chen N, Wells MF, Liu R, Goard MJ, Dimidschstein J, Feng S, Shi Y, Liao W, Lu Z, Fishell G, Moore CI, Feng G (2020) Dysfunction of cortical GABAergic neurons leads to sensory hyper-reactivity in a Shank3 mouse model of ASD. Nat Neurosci 23:520–532.
- Chen TW, Wardill TJ, Sun Y, Pulver SR, Renninger SL, Baohan A, Schreiter ER, Kerr RA, Orger MB, Jayaraman V, Looger LL, Svoboda K, Kim DS (2013) Ultrasensitive fluorescent proteins for imaging neuronal activity. Nature 499:295–300.
- Cole TB, Wenzel HJ, Kafer KE, Schwartzkroin PA, Palmiter RD (1999) Elimination of zinc from synaptic vesicles in the intact mouse brain by disruption of the ZnT3 gene. Proc Natl Acad Sci USA 96:1716–1721.
- Cooke JE, King AJ, Willmore BD, Schnupp JW (2018) Contrast gain control in mouse auditory cortex. J Neurophysiol 120:1872–1884.
- Cooke JE, Kahn MC, Mann EO, King AJ, Schnupp JW, Willmore BD (2020) Contrast gain control occurs independently of both parvalbumin-positive interneuron activity and shunting inhibition in auditory cortex. J Neurophysiol 123:1536–1551.
- Dean I, Harper NS, McAlpine D (2005) Neural population coding of sound level adapts to stimulus statistics. Nat Neurosci 8:1684–1689.
- Harris KD, Shepherd GM (2015) The neocortical circuit: themes and variations. Nat Neurosci 18:170–181.
- Kalappa BI, Tzounopoulos T (2017) Context-dependent modulation of excitatory synaptic strength by synaptically released zinc. eNeuro 4: ENEURO.0011-17.2017.
- Kalappa BI, Anderson CT, Goldberg JM, Lippard SJ, Tzounopoulos T (2015) AMPA receptor inhibition by synaptically released zinc. Proc Natl Acad Sci USA 112:15749–15754.
- Keemink SW, Lowe SC, Pakan JM, Dylda E, Rossum MC, van Rochefort NL (2018) FISSA: a neuropil decontamination toolbox for calcium imaging signals. Sci Rep 8:3493.

- Kerlin AM, Andermann ML, Berezovskii VK, Reid RC (2010) Broadly tuned response properties of diverse inhibitory neuron subtypes in mouse visual cortex. Neuron 67:858–871.
- King AJ, Walker KM (2020) Listening in complex acoustic scenes. Curr Opin Physiol 18:63–72.
- Kouvaros S, Kumar M, Tzounopoulos T (2020) Synaptic zinc enhances inhibition mediated by somatostatin, but not parvalbumin, cells in mouse auditory cortex. Cereb Cortex 30:3895–3909.
- Krall RF, Moutal A, Phillips MB, Asraf H, Johnson JW, Khanna R, Hershfinkel M, Aizenman E, Tzounopoulos T (2020) Synaptic zinc inhibition of NMDA receptors depends on the association of GluN2A with the zinc transporter ZnT1. Sci Adv 6:eabb1515.
- Krall RF, Tzounopoulos T, Aizenman E (2021) The function and regulation of zinc in the brain. Neuroscience 457:235–258.
- Kumar M, Xiong S, Tzounopoulos T, Anderson CT (2019) Fine control of sound frequency tuning and frequency discrimination acuity by synaptic zinc signaling in mouse auditory cortex. J Neurosci 39:854–865.
- Lein ES, et al. (2007) Genome-wide atlas of gene expression in the adult mouse brain. Nature 445:168–176.
- Linden JF, Liu RC, Sahani M, Schreiner CE, Merzenich MM (2003) Spectrotemporal structure of receptive fields in areas AI and AAF of mouse auditory cortex. J Neurophysiol 90:2660–2675.
- Lohse M, Bajo VM, King AJ, Willmore BD (2020) Neural circuits underlying auditory contrast gain control and their perceptual implications. Nat. Commun 11:1–13.
- McAllister BB, Dyck RH (2017a) Zinc transporter 3 (ZnT3) and vesicular zinc in central nervous system function. Neurosci Biobehav Rev 80:329–350
- McAllister BB, Dyck RH (2017b) Sound processing: a new role for zinc in the brain. Elife 6:e31816.
- Nakashima AS, Dyck RH (2009) Zinc and cortical plasticity. Brain Res Rev 59:347–373.
- Olsen SR, Bhandawat V, Wilson RI (2010) Divisive normalization in olfactory population codes. Neuron 66:287–299.
- Pachitariu M, Stringer C, Dipoppa M, Schröder S, Rossi LF, Dalgleish H, Carandini M, Harris KD (2017) Suite2p: beyond 10,000 neurons with standard two-photon microscopy. bioRxiv 061507. doi: 10.1101/061507.
- Palmiter RD, Cole TB, Quaife CJ, Findley SD (1996) ZnT-3, a putative transporter of zinc into synaptic vesicles. Proc Natl Acad Sci USA 93:14934–14939
- Pan E, Zhang X, Huang Z, Krezel A, Zhao M, Tinberg CE, Lippard SJ, McNamara JO (2011) Vesicular zinc promotes presynaptic and inhibits

- postsynaptic long-term potentiation of mossy fiber-CA3 synapse. Neuron 71:1116–1126.
- Paoletti P, Vergnano AM, Barbour B, Casado M (2009) Zinc at glutamatergic synapses. Neuroscience 158:126–136.
- Perez-Rosello T, Anderson CT, Ling C, Lippard SJ, Tzounopoulos T (2015) Tonic zinc inhibits spontaneous firing in dorsal cochlear nucleus principal neurons by enhancing glycinergic neurotransmission. Neurobiol Dis 81:14–19.
- Pnevmatikakis EA, Giovannucci A (2017) NoRMCorre: an online algorithm for piecewise rigid motion correction of calcium imaging data. J Neurosci Methods 291:83–94.
- Rabinowitz NC, Willmore BD, Schnupp JW, King AJ (2011) Contrast gain control in auditory cortex. Neuron 70:1178–1191.
- Rabinowitz NC, Willmore BD, Schnupp JW, King AJ (2012) Spectrotemporal contrast kernels for neurons in primary auditory cortex. J Neurosci 32:11271–11284.
- Romero S, et al. (2020) Cellular and widefield imaging of sound frequency organization in primary and higher order fields of the mouse auditory cortex. Cereb Cortex 30:1603–1622.
- Ruiz A, Walker MC, Fabian-Fine R, Kullmann DM (2004) Endogenous zinc inhibits GABAA receptors in a hippocampal pathway. J Neurophysiol 91:1091–1096.
- Schwartz O, Simoncelli EP (2001) Natural signal statistics and sensory gain control. Nat Neurosci 4:819–825.
- Suter BA, O'Connor T, Iyer V, Petreanu LT, Hooks BM, Kiritani T, Svoboda K, Shepherd GM (2010) Ephus: multipurpose data acquisition software for neuroscience experiments. Front Neural Circuits 4:100.
- Vergnano AM, Rebola N, Savtchenko LP, Pinheiro PS, Casado M, Kieffer BL, Rusakov DA, Mulle C, Paoletti P (2014) Zinc dynamics and action at excitatory synapses. Neuron 82:1101–1114.
- Vogler NW, Betti VM, Goldberg JM, Tzounopoulos T (2020) Mechanisms underlying long-term synaptic zinc plasticity at mouse dorsal cochlear nucleus glutamatergic synapses. J Neurosci 40:4981–4996.
- Wasserman L (2004) Hypothesis testing and p-values. In: All of statistics: a concise course in statistical inference, pp 161–163. New York: Springer.
- Wen B, Wang GI, Dean I, Delgutte B (2009) Dynamic range adaptation to sound level statistics in the auditory nerve. J Neurosci 29:13797–13808.
- Wen B, Wang GI, Dean I, Delgutte B (2012) Time course of dynamic range adaptation in the auditory nerve. J Neurophysiol 108:69–82.
- Wilson NR, Runyan CA, Wang FL, Sur M (2012) Division and subtraction by distinct cortical inhibitory networks in vivo. Nature 488:343–348.